Cryptic crustal growth identified through Variscan post-collisional lamprophyre-granite composite dykes, French Massif Central

Mariana Werle, Gary Stevens, Jean-François Moyen, Oscar Laurent, Chris Harris, Cristiano C. Lana, Philip E. Janney

LITHOS

Cryptic crustal growth identified through Variscan post-collisional lamprophyre-granite composite dykes, French Massif Central.

--Manuscript Draft--

Manuscript Number:	LITHOS11152R1
Article Type:	Regular Article
Keywords:	Composite Dykes; Crustal growth; Variscan Belt; lamprophyre; Metasomatised mantle
Corresponding Author:	Gary Stevens Stellenbosch, SOUTH AFRICA
First Author:	Mariana Werle, MSc
Order of Authors:	Mariana Werle, MSc
	Gary Stevens, PhD
	Jean-François Moyen, PhD
	Oscar Laurent, PhD
	Chris Harris, PhD
	Cristiano Lana, PhD
	Philip Janney, PhD
Abstract:	The processes that control crustal growth by addition of new mantle-derived material to the crust and the recycling of crustal components that were introduced into the mantle during subduction remain poorly understood in collisional orogens. This is largely due to the fact that the sub-orogenic mantle has been fertilized by the introduction of crustal components during previous subduction events, and lacks the typical depleted mantle signature. Here, we present a study of lamprophyric-granitic composite dykes from the northern border of the post-collisional Variscan Aigoual pluton, French Massif Central (FMC). At Aigoual, lamprophyres and granites have gradational contacts and evidences in the field and similar geochemical features that they coexisted indicate that they are comagmatic. U-Pb dating of zircon yields crystallisation ages between 311 ± 2.9 Ma and 313 ± 3.0 Ma for dykes, synchronous within uncertainty with the ages of 312 ± 3.1 Ma and 313 ± 3.2 Ma obtained for the emplacement of the Aigoual pluton. The lamprophyres are metaluminous to slightly peraluminous and display enrichment in both compatible (Fe, Mg, Ni, Cr) and incompatible elements (K 2 O, LILE, LREE) and have crustal isotopic signatures in both radiogenic (Sr, Nd and Hf) and stable (O) isotope systems. This dual crust/mantle signature of the lamprophyres indicates partial melting, within the spinel-lherzolite field, of an enriched mantle that was metasomatised by sediment-derived melts or fluids related to subduction preceding continental collision. The granites are peraluminous, display high K 2 O and have shoshonitic affinities. Their trace elements patterns are similar to the lamprophyres. The isotopic compositions of the granites overlap those of the lamprophyres. The high Cr, Ni, FeO, and MgO contents of the granites are consistent with a mantle component in the magmas. Based on our results, we suggest that between 65 and 80% of material in the lamprophyres and granites was derived from the depleted mantle, and the rest from recycled crustal material. Although blurred from an isotopic point of view, this magmatism contributes with crustal growth in the post-collisional magmatism of the FMC. Coupled with their high preservation potential, post-collisional sites might represent significant sites of crust growth.
Suggested Reviewers:	Jane Scarrow, PhD Professor, University of Granada jscarrow@ugr.es Knowledge on the Variscan belt and igneous petrology.
	Stephen Foley, PhD Professor, Macquarie University

	stephen.foley@mq.edu.au Knowledge in high-K rocks
	Dejan Prelević, PhD Professor, University of Belgrade dejan.prelevic@rgf.bg.ac.rs Knowledge in high-K rocks
	Federico Farina, PhD Professor, University of Milan federico.farina@unimi.it Accomplished granite petrologist
	Simon Couzinie, PhD Researcher, UL University SIMON.COUZINIE@GMAIL.COM Has worked extensively in the region
	Marc Poujol, PhD Professor, University of Rennes marc.poujol@univ-rennes.fr Accomplished geochronologist with an interest in crustal evolution
Opposed Reviewers:	

Title: **Cryptic crustal growth identified through Variscan post-collisional lamprophyre-granite composite dykes, French Massif Central**

Mariana Werle[a], Gary Stevens[a*], Jean-François Moyen[b], Oscar Laurent[c], Chris Harris[d], Cristiano C. Lana[e], Philip E. Janney[d]

* Corresponding author

[a] Stellenbosch University, Department of Earth Sciences, Private Bag X1, 7602 Matieland, South Africa

[b] Université de Lyon, Laboratoire Magmas et Volcans, UJM-UCA-CNRS-IRD, 23, rue Dr. Paul Michelon, 42023 Saint-Étienne, France

[c] GET, UPS, CNRS, IRD, 14, avenue E. Belin, F-31400 Toulouse, France

[d] University of Cape Town, Department of Geological Sciences, Rondebosch, 7700, South Africa

[e] Universidade Federal de Ouro Preto, Departamento de Geologia, Escola de Minas, Morro do Cruzeiro, 35400-000, Ouro Preto, Minas Gerais, Brazil

Abstract

The processes that control crustal growth by addition of new mantle-derived material to the crust and the recycling of crustal components that were introduced into the mantle during subduction remain poorly understood in collisional orogens. This is largely due to the fact that the sub-orogenic mantle has, in many instances, been fertilized by the introduction of crustal components during previous subduction events, and lacks the typical depleted mantle signature. Here, we present a study of lamprophyric–granitic composite dykes from the northern margin of the post-collisional Variscan Aigoual granite, French Massif Central (FMC). At Aigoual, lamprophyres and granites have gradational contacts and similar geochemical characteristics which indicate that the two were co-magmatic. U–Pb dating of zircon yields crystallisation ages between 311 ± 3 Ma and 313 ± 3 Ma for dykes, identical within uncertainty with the ages of 312 ± 3 Ma and 313 ± 3 Ma obtained for the emplacement of the Aigoual granite. The lamprophyres are metaluminous to slightly peraluminous and display enrichment in both compatible (Fe, Mg, Ni, Cr) and incompatible elements (K_2O, LILE, LREE) and have crustal isotopic signatures in both radiogenic (Sr, Nd and Hf) and stable (O) isotope systems. This dual crust/mantle signature of the lamprophyres can be interpreted as partial melting, within the spinel stability field, of an enriched mantle that was metasomatised by the addition of subducted sediments. The granites are peraluminous, display high K_2O and have shoshonitic affinities. Their primitive mantle-normalized trace-element patterns are similar to the lamprophyres and the isotopic compositions of the two rock types overlap. The high Cr, Ni, FeO, and MgO contents of the granites are consistent with a mantle component in the magmas. Our results suggest that between 65 and 80 wt% of material in the lamprophyres and granites was derived from the depleted mantle, and the rest from recycled crustal material. Although blurred from an (conventional) isotopic point of

view, this magmatism contributed to the crustal growth via the post-collisional magmatism of the FMC. Coupled with their high preservation potential, post-collisional sites might thus represent significant sites of crustal growth.

Keywords: Composite Dykes; Crustal Growth; Variscan Belt; Lamprophyre; Metasomatised mantle

Highlights

- Lamprophyre-granite composite dykes from late-Variscan Aigoual pluton, French Massif Central;
- Mantle-crust interaction in a post-collisional setting;
- Sr-Nd-Hf and O isotopes display a cryptic crustal growth.

Title: **Cryptic crustal growth identified through Variscan post-collisional lamprophyre-granite composite dykes, French Massif Central**

Mariana Werle[a], Gary Stevens[a*], Jean-François Moyen[b], Oscar Laurent[c], Chris Harris[d], Cristiano C. Lana[e], Philip E. Janney[d]

* Corresponding author

[a] Stellenbosch University, Department of Earth Sciences, Private Bag X1, 7602 Matieland, South Africa

[b] Université de Lyon, Laboratoire Magmas et Volcans, UJM-UCA-CNRS-IRD, 23, rue Dr. Paul Michelon, 42023 Saint-Étienne, France

[c] GET, UPS, CNRS, IRD, 14, avenue E. Belin, F-31400 Toulouse, France

[d] University of Cape Town, Department of Geological Sciences, Rondebosch, 7700, South Africa

[e] Universidade Federal de Ouro Preto, Departamento de Geologia, Escola de Minas, Morro do Cruzeiro, 35400-000, Ouro Preto, Minas Gerais, Brazil

Abstract

The processes that control crustal growth by addition of new mantle-derived material to the crust and the recycling of crustal components that were introduced into the mantle during subduction remain poorly understood in collisional orogens. This is largely due to the fact that the sub-orogenic mantle has, in many instances, been fertilized by the introduction of crustal components during previous subduction events, and lacks the typical depleted mantle signature. Here, we present a study of lamprophyric–granitic composite dykes from the northern margin of the post-collisional Variscan Aigoual granite, French Massif Central (FMC). At Aigoual, lamprophyres and granites have gradational contacts and similar geochemical characteristics which indicate that the two were co-magmatic. U–Pb dating of zircon yields crystallisation ages between 311 ± 3 Ma and 313 ± 3 Ma for dykes, identical within uncertainty with the ages of 312 ± 3 Ma and 313 ± 3 Ma obtained for the emplacement of the Aigoual granite. The lamprophyres are metaluminous to slightly peraluminous and display enrichment in both compatible (Fe, Mg, Ni, Cr) and incompatible elements (K_2O, LILE, LREE) and have crustal isotopic signatures in both radiogenic (Sr, Nd and Hf) and stable (O) isotope systems. This dual crust/mantle signature of the lamprophyres can be interpreted as partial melting, within the spinel stability field, of an enriched mantle that was metasomatised by the addition of subducted sediments. The granites are peraluminous, display high K_2O and have shoshonitic affinities. Their primitive mantle-normalized trace-element patterns are similar to the lamprophyres and the isotopic compositions of the two rock types overlap. The high Cr, Ni, FeO, and MgO contents of the granites are consistent with a mantle component in the magmas. Our results suggest that between 65 and 80 wt% of material in the lamprophyres and granites was derived from the depleted mantle, and the rest from recycled crustal material. Although blurred from an (conventional) isotopic point of

view, this magmatism contributed to the crustal growth via the post-collisional magmatism of the FMC. Coupled with their high preservation potential, post-collisional sites might thus represent significant sites of crustal growth.

Keywords: Composite Dykes; Crustal Growth; Variscan Belt; Lamprophyre; Metasomatised mantle

1. Introduction

The process that allow continental crust to be generated and evolve involve the addition of new, mantle-derived magma to the crust; the recycling and melting of oceanic crust and sediments at subduction sites and the addition of these magmas to the continental crust; as well as the anatectic reworking of the continental crust in collisional environments (Dhuime et al., 2011; Jacob et al., 2021; Moyen et al., 2021). The continental crust grows when new, purely mantle-derived material is added to the continents, not when continental crustal components introduced into the mantle are returned to the crust; this is simply crust coming home. Growth of the continental crustal occurred extensively in arc settings throughout geological time, where large amounts of mantle-derived mafic and intermediate magmas (and their differentiates) were added to the crust. Nevertheless, this does not necessarily imply significant long-term crustal-growth, because arc settings display poor preservation potential. A high proportion of the crust generated in this setting may be recycled back to the mantle shortly after formation (Kay and Kay, 1993; Condie, 2014; Scholl and von Huene, 2009). Although less efficient than arc settings in producing new continental crust, post-collisional sites display the greatest potential for preservation in the geological record (Hawkesworth et al., 2009; Spencer et al., 2015). Post-collisional settings are characterized by orogenic collapse, potential delamination of the lithosphere and hence asthenospheric upwelling. This may produce a range of magmas, including granites, from both mantle and crustal sources (Bonin, 2004; Clemens et al., 2009). Thus, post-collisional settings represent a significant opportunity for crustal growth in an environment with potential for long-term preservation (Couzinié et al., 2016; Moyen et al., 2017; Gómez-Frutos et al., 2023).

In this context, high-K–Mg mantle-derived magmatic suites occur systematically in post-collisional settings. Although relatively scarce, the suites are considered a significant contributor to crustal growth throughout geological time (Prelević et al., 2012; Scarrow et al., 2008; Murphy, 2020). Post-collisional high-K–Mg mafic rocks have been described in the Variscan belt of Western Europe (e.g. Turpin et al., 1988; Janoušek & Holub, 2007; Couzinié et al., 2016; von Raumer et al., 2014). These rocks are characterized by a significant range of SiO_2 contents (45–65 wt%), high-K, through shoshonitic to ultrapotassic affinity (K_2O = 1.5-6.0 wt%), and high maficity (FeOt + MgO up to 25 wt%). They are enriched in volatiles, mantle-compatible (Mg, Ni, Cr) and incompatible elements (e.g., K, Rb, Ba, Sr).

The French Massif Central is a segment of the Variscan Belt, in which high-K–Mg mafic rocks are spatially and temporally associated with the peak of granite magmatism (335 to 300 Ma; Couzinié et al., 2014; Laurent et al., 2017). These mafic rocks occur as either enclaves to decametric small bodies in felsic igneous rocks and migmatites, or as lamprophyric dykes (Couzinié et al., 2014; 2016; Sabatier, 1991). Despite being well defined in space and time, the role of this mafic magmatism in the post-orogenic phase of the Variscan orogeny is still debated (e.g. Tabaud et al., 2015; Couzinié et al., 2016). More specifically, it is unclear whether the volumetrically more significant granites represent differentiated magmas from the mafic rocks (Clemens et al., 2021; Moyen et al., 2017) or the products of hybridization between the mafic and crustal melts (Laurent et al., 2017, Solgadi et al., 2007, Yamasaki, 2022). In turn, the balance between crustal growth by addition of new mantle-derived material and crustal recycling into the mantle in post-collisional sites is poorly understood (Jacob et al., 2021; Storck et al., 2021, and references therein). To contribute to this debate, we selected co-magmatic lamprophyres and granites in a unique system of parallel dykes associated with the northern boundary of the late-

Variscan Aigoual granite, French Massif Central, to investigate the petrogenesis of both rock types, explore the potential genetic links between them and to constrain the contribution of mantle-derived material to these post-collisional magmas.

2. Geological setting

2.1 The French Massif Central

The orogenic Variscan Belt in central and Western Europe formed between c. 400 and 280 Ma in a complex history of collision between two main continents, Gondwana and Laurussia, as well as intervening micro-continents and oceanic basins, resulting in the formation of the Pangea supercontinent at the end of the Paleozoic (Kröner and Romer, 2013; Stampfli et al., 2013; Matte, 2001). One of the largest exposures of the Variscan Belt in Western Europe is preserved in the French Massif Central (FMC) (Vanderhaeghe et al., 2020). Igneous and metamorphic rocks here represent the exhumed root zone of the orogen (Lardeaux et al., 2014), constructed over the northern margin of Gondwana (Fig. 1b).

From the Ordovician to the late Carboniferous, the FMC experienced several tectonometamorphic–magmatic events, with opening of ocean basins (ca. 500–450 Ma) and subsequently closure and subduction between 420 and 360 Ma, to continental collision between ca. 350 and 320 Ma. Orogenic collapse occurred in the late Carboniferous (ca. 320–300 Ma) (Faure et al., 2009; Vanderhaeghe et al., 2020). The eastern FMC (E-FMC) consists of a south-verging stack of nappes that are composed of four main metamorphic units (Faure et al., 2009; Vanderhaeghe et al., 2020).

In the southeastern part of the FMC, a low-grade metamorphic unit called the Parautochthonous Unit represents the lowermost unit of the nappe pile. It exposes predominantly metasediments (micaschists, quartzites and graphitic metapelites) (Faure et al., 1999) deposited

between the Neoproterozoic and early Cambrian (Melleton et al., 2010), minor orthogneisses formed in the late Cambrian to Early Ordovician (490–485 Ma), and metarhyolites. These rocks underwent polyphase deformation and metamorphism between ca. 340 and 310 Ma under greenschist- to amphibolite-facies conditions (Faure et al., 1999) (Fig. 1b). This unit was intruded by the Aigoual–Saint Guiral–Liron Pluton (ASGL) at shallow depth (1–2 kbar; Najoui et al., 2000) developing a contact metamorphic aureole. Based on U–Pb dating in zircon and monazite, and $^{40}Ar/^{39}Ar$ dating in biotite, the main intrusion occurred between 305 and 310 Ma. Thus it was synchronous with the late stage of migmatization at lower structural levels and the late Variscan extensional event in this area (Brichau et al., 2008).

2.2 Magmatic relations in the E-FMC and Aigoual granite

The main phase of igneous activity in the French Massif Central occurred during the transition from mid-Carboniferous collision to the syn- and post-orogenic collapse of the orogen in late-Carboniferous to early-Permian times (Faure et al., 2009; Laurent et al., 2017). The plutonic rocks of E-FMC can be subdivided in four main groups (Chantraine et al., 1996; Barbarin, 1999). (1) Two-mica or muscovite-bearing peraluminous granitoids ("MPG") cropping out as small plutons and dykes. These rocks are granites *sensu stricto* with SiO_2 (>70 wt%); their chemistry and isotopic characters indicate mature crustal source (Pin and Duthou, 1990); (2) Cordierite-bearing peraluminous granitoids ("CPG"), which are granodiorites to granites with biotite and cordierite ranging from abundant to rare. These rocks are characterized by K_2O contents in the range of 3–7 wt%, with SiO_2 > 65wt%. Isotopic characteristics suggest melting of local crust as the source of the magmas that formed these rocks (Pin and Duthou, 1990; Williamson et al., 1992). The compositions of the CPG are consistent with higher melting temperatures (≥ 850 ºC, biotite breakdown) than the MPG (Laurent et al., 2017; Villaros et al.,

2018) and/or greater proportions of orthogneisses in the source (Downes et al., 1997; Moyen et al., 2017), although with limits imposed by their isotopic compositions. (3) K-feldspar-phyric, biotite ± amphibole-bearing granites, granodiorites and quartz diorites ("KCG") are high-K calc-alkaline, metaluminous to weakly peraluminous and form large plutons (e.g., Aigoual–Saint Guiral–Liron) or enclaves in the Velay Complex. In general, they are more mafic than the CPG, having $FeO^t + MgO \sim 4$ wt%, with SiO_2 contents averaging around 69 wt%. (4) A suite of biotite–amphibole ± clinopyroxene-bearing mafic to intermediate rocks that occur throughout the Variscan Belt (von Raumer et al., 2014) and are locally known as vaugnerites (Couzinié et al., 2016; Sabatier, 1991). The vaugnerites are metaluminous with low silica ($44 < SiO_2 < 63$ wt%), high $FeO^t + MgO$ (10–24 wt%), Cr (200–600 ppm) and Ni (100–220 ppm) contents, Mg# (molecular $Mg/(Mg + Fe) > 0.65$. They also have high K_2O contents (1.6–6.7 wt%) and high Ba and Sr contents (1000–2000 ppm; Couzinié et al., 2016). In this contribution, we refer to these rocks as lamprophyres.

The Aigoual granite forms the northern end of the L-shaped Aigoual-Saint Guiral-Liron (AGSL) Pluton in the southeastern FMC. The ASGL rocks are classified as K-feldspar-phyric calc-alkaline granitoids (KCG) (Chantraine et al., 1996). The northern termination of the Aigoual granite consists of a swarm of NE–SW to NNE–SSW-trending lamprophyre–granite composite dykes, which are the subject of this study (Fig. 1c).

3. Analytical methods

This study has integrated information on field relations, petrography, mineral chemistry, whole-rock major and trace element compositions, whole-rock Nd, Sr and Hf isotopic ratios, U–Pb dating and Lu–Hf analyses in zircon and oxygen isotopes in quartz and K-feldspar, from the Aigoual lamprophyre-granite composite dykes and three samples from the Aigoual granite. The

whole-rock major- and trace-element data information of mineral major element compositions, as well as U–Pb dating of zircon, were undertaken at the Central Analytical Facilities at Stellenbosch University, South Africa. The whole-rock Nd, Sr and Hf isotope analyses and quartz and K-feldspar oxygen isotope ratio analyses were undertaken at the University of Cape Town. Lu–Hf analyses in zircon were carried out at Universidade Federal de Ouro Preto, Brazil. The analytical details for each method are described in the Supplementary Material 1.

4. Results

4.1 Field relations

At the northern end of the Aigoual granite, several 100–1000 m long, NE-trending dykes intrude the Cévennes micaschists, part of the Parautochthonous Unit described above. Most dykes are composite and display gradation between granitic and lamprophyric components. The wider dykes (described by Sabourdy, 1975) display lamprophyric dark borders with aphanitic textures, progressively grading into porphyritic microgranites with some mafic enclaves in the cores. In general, bulk compositional gradients that are interpreted to reflect different mixing ratios, are aligned parallel to the dyke walls. The dyke illustrated in Fig. 2a varies from lamprophyre to granite (SiO_2 57.20 to 67.81 wt%) from left to right in the image. An increase in number and size of K-feldspar phenocrysts, from lamprophyric to granitic end-members, was observed in the field (Fig. 2a). In other outcrops, lamprophyric and granitic components form independent dykes that were observed to intrude one another (Fig. 2b).

The Aigoual granite proper contains many typically rounded, 1 to 3dm in diameter (Fig. 2c), lamprophyric enclaves with partly resorbed phenocrysts of K-feldspar. In combination, the compositionally gradational dykes and the existence of lamprophyric enclaves in the granites that include crystals likely to have been captured from the granite magma. In combination, this

mineral textural and field evidence demonstrates the coeval nature of the granitic and lamprophyric magmas.

The sample list and the coordinates of the sample points are presented in Supplementary Data 2.

4.2 Petrography and mineral chemistry

4.2.1 The composite dykes

The lamprophyres have panidiomorphic–porphyritic textures with phenocrysts of euhedral biotite (~ 25–30 vol%), plagioclase (~ 20%), quartz (~ 5%) and K-feldspar (~ 5%), set in a fine matrix composed of quartz, alkali-feldspar, plagioclase, biotite, ± amphibole, ± carbonate (Fig. 3). Olivine and pyroxene were not observed but pseudomorphs indicate the former presence of one or more ferromagnesian phases in some lamprophyric samples, as also reported by Sabourdy (1975) from the same outcrops. Accessory minerals are apatite, zircon, ilmenite, ± allanite, ± rutile.

A characteristic of the lamprophyres is the presence of carbonate in three different textural forms (Fig. 3): 1) globular, ocellar; 2) interstitial to the silicate minerals, and 3), intergrown with biotite/phlogopite. The carbonate-mica intergrowths appear to pseudomorph a prior blocky mineral.

Carbonate (dolomite) was observed mantling corroded quartz that varies from 0.4 to 0.6 mm in size (Supplementary Figure 1a). Ocellar carbonate aggregates vary from 0.2–1.6 mm in diameter; the ocelli also contain very fine-grained alkali-feldspar (Fig. 3). The matrix surrounding the ocelli is aphanitic and composed of quartz, plagioclase, biotite (partially altered to chlorite in some places). Matrix plagioclase laths display an orientation tangential to the

margins of the carbonate globules indicating that the ocelli structures formed part of the magma (Supplementary Figure 1b-c). Interstitial carbonate is present among euhedral quartz, plagioclase and biotite (Supplementary Figure 1d). The interstitial character of the carbonate relative to euhedral quartz, biotite and plagioclase crystals is shown in the Si X-ray map of Supplementary Figure 1e. Plagioclase crystals associated with the carbonate display normal magmatic zoning with Na content increasing towards the rim (Ab_{56} to Ab_{75}) (Supplementary Figure 1f). The carbonate associated with biotite/phlogopite (interpreted as pseudomorphing a high-temperature ferromagnesian phase) was observed in both granitic and lamprophyric samples (Supplementary Figure 1g, h). In these textures, calcite or dolomite cores are rimmed by blocky phlogopite and both replace a former phenocryst with rectangular habit, possibly pyroxene.

Granitic samples from composite dykes display seriate porphyritic textures with extreme average crystal size variations between the phenocrysts and the matrix. In general, the phenocrysts (up to 5 cm) of plagioclase (~ 30%), K-feldspar (~ 30%), quartz (~ 20%) biotite (~ 5–10%) and ± clinopyroxene (~ 3%) are set in a fine- to medium-grained matrix composed of quartz, K-feldspar ± plagioclase. Accessories are apatite, zircon, ± allanite, ± titanite ± ilmenite. In some samples, phenocrysts of plagioclase display oscillatory zoning (Fig. 3j) and some K-feldspar phenocrysts have corroded margins (Fig. 3l).

4.2.2 Aigoual granite

The Aigoual granite proper consists predominantly of strongly porphyritic, coarse-grained granite with phenocrysts of K-feldspar reaching 5–8 cm. The granite contains phenocrysts of K-feldspar (~ 30%), plagioclase (~ 20%) and quartz (~ 15%) in a coarse matrix of quartz, plagioclase and K-feldspar (~20%), mica (~7%) and clinopyroxene (~5%).

4.2.4 Mineral Chemistry

Mineral chemistry data is presented in Supplementary Data 4, Table S1. Euhedral crystals of mica from the lamprophyres have Mg# varying from 0.47 to 0.80, corresponding to a transition between biotite (Mg# < 0.65) and phlogopite (Mg# > 0.65) (Fig. 4a). Biotite/phlogopite has low to moderate Cr_2O_3 content (0–0.05 apfu), high Ti (0.37–0.97 apfu) and in some samples displays zoning in BSE images with dark grey cores and light gray discordant rims (e.g. Fig. 3g). The cores have lower Ti (0.42–0.59 apfu) than the rims (0.78–0.97 apfu) and biotite in the matrix shows similar compositions to the rims with high Ti (0.69–0.94 apfu). In the FeO^t vs. Al_2O_3 and TiO_2 vs. Al_2O_3 mica discrimination diagrams, the biotite/phlogopite follows a minette trend, typical of calc-alkaline lamprophyres (Fig. 4b–c; Rock, 1991). Dark micas in the granites from the composite dykes are generally less magnesian than those in the lamprophyres, with an average of Mg# ~ 0.52 and are thus classified as biotite. A few analyses with Mg# > 0.65 fall in the phlogopite field (Fig. 4a). Biotite in the Aigoual granite proper has Mg# ~ 0.52.

Feldspar compositions are illustrated in Supplementary Figure 2a. Feldspar in the lamprophyres is predominantly plagioclase, which ranges in composition from An10 to An60. Alkali feldspar is a relatively minor component in these rocks and ranges in composition from Or5 to Or40. Feldspar in the Aigoual granite consist of plagioclase with a narrow compositional range clustered around An30 and K- feldspar which varies in composition from Or80 and 92. In the granite dykes the plagioclase compositional range is similar to that exhibited by the lampropyric dykes. However, at low An contents significantly more K_2O (typically up to Or30) is present in some feldspar crystals with significant Ca, which plot in the fields of oligoclase and anorthoclase. The more common alkali-feldspar compositions in these dykes vary from Or60 to Or100.

All pyroxene in the Aigoual granite and in the granitic dykes is augite and clusters in a narrow range of compositions characterized by Ca contents in the range of Di50 to 60 and with Mg#s between 60 and 75 (Supplementary Fig. 2b). All amphibole from the lamprophyres is actinolite with high Si contents (7.53–7.90 apfu) and Mg# (0.62–0.88), as is typical of secondary amphiboles in lamprophyres (Supplementary Fig. 2c and d).

4.3 Zircon U–Pb ages and Lu–Hf isotopes

In this work, the geochronological data are from individual composite dykes, where lamprophyre and granite occur in the same outcrop with gradational transition from one to the other. The zircons are euhedral to subhedral, 50–450 µm across. The crystals have prismatic, subrounded prismatic, pyramidal to bipyramidal tips and aspect ratios from 4:1 to 1:1. Under CL, they exhibit strong to weak oscillatory zoning, diffuse zoning or no luminescence at all (Supplementary Figure. 3). Many grains show a core–rim texture with diffusely or oscillatory zoned core surrounded by a dark rim. Inherited cores display bright, diffuse to oscillatory, truncated zoning with dark rims.

The $^{206}Pb/^{238}U$ dates show a large range of concordant ages, scattering from 340 to 300 Ma (Fig. 5). However, this large dispersion displays no correlation with position of the analysis spot in different zircon crystals. Older ages, between 320 and 340 Ma, were obtained from both dark rims and CL-dark grain interiors with unusually high U contents (> 1000 ppm). Due to the high U content, these zircons might no longer be crystalline (Ewing et al., 2003). The absence of a correlation between age and Hf isotopic composition indicates that the age dispersion has no geological significance. The older ages, between 320 and 340 Ma, are likely to be artefacts potentially caused by inaccurate correction for downhole fractionation in these high U crystals and strongly radiation damaged zircon. Accordingly, the Concordia ages were calculated using

data from zircons that were more likely to retain coherent crystallinity (U < 1000 ppm) and KDE variation, which displays a peak at 315 - 310–Ma for most of the samples (Fig. 6).

Eleven concordant analyses from lamprophyres and granites of dyke 5 yielded a Concordia date of $^{206}Pb/^{238}U$ = 313 ± 3 Ma (MSWD conc. + equiv. = 1.7) (Fig. 5a). Inherited grains were largely found in the granite component and yielded $^{206}Pb/^{238}U$ ages of = 537 ± 10, 541 ± 14, 545 ± 9, 649 ± 10 and 673 ± 7 Ma. Younger ages of 296 ± 4 and 291 ± 5 Ma are interpreted as reflecting Pb loss. Magmatic zircons from dyke 5 have $\varepsilon\frac{Hf}{311}$ = –1.6 to–8.1 (± 1.2), T_{DM} = 1.7 to 1.3 Ga] (Fig. 6). The inherited zircons yielded $\varepsilon\frac{Hf}{311}$ of +6.8 to +0.9.

Thirty-three concordant analyses from lamprophyres and granites of dyke 10 yielded a Concordia date of $^{206}Pb/^{238}U$ = 311 ± 3 Ma (MSWD conc. + equiv. = 1.5) (Fig. 5b). A large population of inherited grains found in the granite component yielded several date groups from Paleoproterozoic (2490-2040 to 2480 Ma), through early Neoproterozoic (920–1000 Ma) to late Neoproterozoic and early Paleozoic (450–730 Ma). Zircons from dyke 10 have $\varepsilon\frac{Hf}{311}$ = +3.6 to –7.7 (± 1.5) (Fig. 6), with T_{DM} = 1.7 to 1.1 Ga. Inherited grains with $^{206}Pb/^{238}U$ ages of 450–600 Ma gave $\varepsilon\frac{Hf}{311}$ of +2.5 to 0.0, whereas inherited grains (> 600 Ma) yielded $\varepsilon\frac{Hf}{311}$ of +2.9 –13.5.

Samples 12A and 12B represent the eastern margin of Aigoual granite with microgranite and monzonite occurring as part of the body of the granite, in contrast to all the other granite samples, which form part of the composite dykes. Isotopic data from 10 concordant analyses display a Concordia date of 312 ± 3 Ma (MSWD conc. + equiv. = 1.7) (Fig. 8c). No inherited grains were observed. Zircon grains from margin of Aigoual granite (locality 12) have $\varepsilon\frac{Hf}{311}$ = 0.4 to –6.8 (± 1.4), T_{DM} = 1.6 to 1.2–Ga] (Fig. 6).

296 Zircons from the Aigoual granite proper yield a Concordia date of 313 ± 3 Ma (MSWD conc.
297 + equiv. = 1.3; n = 7) (Fig. 8d) with ε_{311}^{Hf} = –5.6 to –3.3 (± 1.1), T_{DM} = 1.4–1.5 Ga] (Fig. 6).

298 **4.4 Whole-rock major- and trace-element chemistry**

299 In the TAS system of Le Maitre et al. (2002), the rocks of this study would be classified as
300 granites, quartz monzonites and monzonites, but of course such alkali rick compositions are not
301 amenable to classification according composition discrimination diagrams. The compositions of
302 the three Aigoual granite samples are very similar and fall consistently between the compositions
303 of the granitic and lamprophyric portions of the composite dykes on plots of all elements vs. SiO_2
304 (Fig. 7). The dykes show a wide range in SiO_2, varying from 53.16 to 72.57 wt%, recalculated on
305 a volatile-free basis. Lamprophyric and granitic samples are high-K (4.08–6.55 wt%) with
306 shoshonitic affinities (Fig. 8a) and high Al_2O_3 (13.63–17.18 wt%). In the A/NK vs. A/CNK
307 [molar $Al_2O_3/(Na_2O + K_2O)$ vs. $Al_2O_3/(CaO + Na_2O + K_2O)$] diagram of Shand (1943),
308 lamprophyric samples classify as metaluminous to slightly peraluminous with higher A/NK
309 values, whereas granitic samples are weakly to moderately peraluminous with some exceptional
310 cases having A/CNK > 1.3 (Fig. 8b).

311 A striking feature of the bulk rock chemistry of the entire sample set is that Cr, Ni and Ba are
312 high (30–573 ppm, 15–149 ppm and 404–2416 ppm, respectively), but variable and with only a
313 vague inverse correlation with SiO_2. Mg# varies from 41 to 71 and along with TiO_2 and P_2O_5 is
314 one of the components which shows the best developed inverse correlation with SiO_2
315 concentration. For the incompatible elements, which commonly are positively correlated with
316 SiO_2 content, Na_2O demonstrates this behavior, despite a significant amount of scatter, for the
317 lamprophyres. However, for the granites, if there is any trend its flat. Similarly, over the whole

range of compositions K_2O shows no correlation with SiO_2, with the majority of the rocks falling between 5 and 6 wt% K_2O.

The lamprophyric–granitic rocks from composite dykes and the Aigoual granite are enriched in large ion lithophile elements (LILE, e.g. Cs, Rb, Ba, Th, U; Fig. 9a) and Pb relative to high field strength elements (HFSE, e.g. Nb, Ta, P, Zr and Ti). The lamprophyres show negative Nb, Ta and Ti anomalies, but Ta anomalies are not observed in the granites. In general, the lamprophyres are richer in REE and mantle-incompatible elements than the granites, as is commonly observed in these types of rocks (e.g. Couzinié et al., 2016; Fowler et al., 1996).

In the primitive mantle -normalized (Sun and McDonough 1989) REE multielement plot (Fig. 9b), lamprophyres and granites from composite dykes as well as the Aigoual granite samples show similar patterns. They are enriched in LREE (La_N = 24–147) and depleted in HREE (La_N/Yb_N = 3.34–22.81). In general, lamprophyres show smaller negative Eu anomalies (Eu/Eu* = 0.60–0.85) than granites (Eu/Eu* = 0.38–0.86).

4.5 Whole-rock Sr–Nd–Hf isotopes

Lamprophyres and granites from the composite dykes show little variation in Sr, Nd and Hf isotope ratios. Initial $^{87}Sr/^{86}Sr$ ratios of lamprophyres and granites overlap and vary from 0.7080 to 0.7106. Similarly, the Nd isotope ratios of the lamprophyres and granites overlap (ε_{311}^{Nd} = –3.60 to –5.39 and ε_{311}^{Nd} = –4.62 to –5.39 respectively). The Hf isotope ratios for both rock types also overlap, with lamprophyres varying from ε_{311}^{Hf} = –0.26 to –4.92 and [the] granites varying from ε_{311}^{Hf} = –2.31 to–3.47 (Fig. 14) (Table S2 from Supplementary Data 3). On average, lamprophyres have slightly more radiogenic Nd and Hf than granites (ε_{311}^{Nd} = -4.40 and -5.13, and

340 ε_{311}^{Hf} = -2.81 and -3.20, respectively). The Aigoual granite has an ($^{87}Sr/^{86}Sr)_i$ of 0.70941, ε_{311}^{Nd} = –

341 5.43 and ε_{311}^{Hf} = –3.71.

342 **4.6 Quartz, and K-feldspar O isotopes**

343 The $\delta^{18}O$ values of quartz and K-feldspar ($\delta^{18}O_{Qtz}$ and $\delta^{18}O_{Fsp}$ respectively) from composite

344 dykes are listed in Table 3 from Supplementary Data 4 and illustrated in Fig. 10. The $\delta^{18}O_{Qtz}$

345 values vary from 10.76 to 11.21‰ (n = 9; average = 10.97‰) and, despite their narrow range,

346 show a positive correlation with whole-rock SiO_2 (r^2 = 0.72) (Fig. 10a) and a negative one with

347 Cr + Ni (r^2 = –0.66) (Fig. 10b). The $\delta^{18}O_{Fsp}$ vary from 6.4 to 13‰ (n = 9; average = 9.4‰) and

348 are thus much more variable than for quartz. There is no correlation between $\delta^{18}O_{Fsp}$ and $\delta^{18}O_{Qtz}$

349 (Fig. 10c). The $\delta^{18}O_{Qtz}$ values display no correlation with whole-rock ($^{87}Sr/^{86}Sr)_i$ (r^2 = 0.13) (Fig.

350 10d), ε^{Nd} (r^2 = 0.17; not shown) and ε^{Hf} (r^2 = 0.23; not shown). The three lamprophyre samples

351 plot between the diffusion closure and crystallization isotherms on a δ–δ plot (Fig. 10c). The

352 remaining samples show a wide range in feldspar $\delta^{18}O$ values that are both higher and lower than

353 $\delta^{18}O_{Qtz}$. The wide range in $\delta^{18}O_{Fsp}$ values is consistent with interaction with fluids at a range of

354 temperatures.

355 # 5. Discussion

356 **5.1 Timing of magma emplacement**

357 U–Pb analyses in zircon from lamprophyres and granites from dykes 5 and 10 yielded

358 $^{206}Pb/^{238}U$ ages of 313 ± 3 Ma and 311 ± 3 Ma, respectively. Locality 12, in the Aigoual granite

359 at its eastern border, gave a $^{206}Pb/^{238}U$ age of 312 ± 3 Ma and the granite from the center of the

360 body has a $^{206}Pb/^{238}U$ age of 313 ± 3 Ma. Therefore, all samples of dykes and the Aigoual granite

361 show the same crystallization ages, within uncertainties. These are statistically indistinguishable

362 from the U–Pb age of 304 ± 12 Ma, reported by Brichau et al. (2008), from the southern portion
363 of the ASGL Pluton.

364 The alignment of the high-K–Mg rocks in FMC in along NE–SW trends (Fig. 1b), that are
365 also parallel to major lithological boundaries, suggests that emplacement followed zones of
366 weakness in the crust. Emplacement was possibly also facilitated by NW–SE directed
367 extensional associated with crustal thinning of the Variscan Belt, during the syn- to post-
368 collisional period (Faure et al., 2009; Talbot et al., 2005). Dykes from northern Aigoual granite
369 display an AMS fabric indicative of NE–SW stretching. However, this fabric was controlled by
370 magmatic flow rather than regional extension, suggesting a southwestward source feeding the
371 magmatic system (Talbot et al., 2005).

372 The lack of inherited or xenocrystic zircon grains in lamprophyres can be explained by
373 zircon under-saturation due to the high temperature and mafic composition of these magmas
374 (Laurent et al., 2017). Inherited grains in granitic samples display a wide spread of
375 Paleoproterozoic to late-Ordovician ages (Fig. 8b) and ε^{Hf} signatures from -13 to +6.8, consistent
376 with age distribution and isotopic signatures from Variscan ortho- and paragneisses in the FMC
377 (Chelle-Michou et al., 2017).

378 Dating of granites that were proposed to be crustally derived and mantle-derived mafic
379 magmas in the E-FMC (Couzinié et al., 2014; Laurent et al., 2017) showed that the two were
380 related in space and time. They marked a protracted (40 Myr) magmatic period, in which granites
381 (337 ± 1 to 299 ± 2 Ma), emplaced coevally with vaugnerites (336 ± 2 and 299 ± 1 Ma – Laurent
382 et al., 2017). The age distribution displays migration of magmatism toward the south, where the
383 younger ages of 307 and 298 Ma were reported from the KCG plutons in the Cévennes area
384 (Couzinié et al., 2014; Laurent et al., 2017). These are substantially younger than the ages

reported in the current work. Late Carboniferous southward delamination of the lithospheric mantle and asthenosphere upwelling may explain the long-lived lithospheric-scale thermal anomaly that could have produced melts of both crustal and mantle sources (Laurent et al., 2017).

5.2 Origin of the lamprophyres and granites

5.2.1 Origin of lamprophyres

The lamprophyres have moderate to high compatible element contents, e.g. Cr (74–572 ppm) and Ni (23–148 ppm), coupled with relatively high Mg# (up to ~ 70), consistent with a mantle source for at least this component of the composite system. However, the lamprophyres also display elevated concentrations in LILE (K_2O, Sr, Rb, Ba,), LREE and depletion in HFSE such Nb, Ta and Ti, in relation to the primitive mantle. Whole-rock Sr–Nd–Hf and in-zircon Hf isotopes display crust-like signatures with subchondritic ε^{Nd} and ε^{Hf} values. Also the $\delta^{18}O$ values for the lamprophyres are on average 5‰ higher than the expected value for depleted mantle (5.2‰, Eiler, 2001). The crust-like signatures of the lamprophyres can result from crustal assimilation accompanying fractional crystallization of a primitive basaltic liquid (AFC process) or partial melting of an enriched mantle source, that was metasomatised by interaction with crustal material during the subduction stage that preceded the continental collision (e.g., Becker et al., 1999; Janoušek and Holub, 2007; Lexa et al., 2011; Schulmann et al., 2014; Couzinié et al., 2016).

The absence of correlations between Mg#, Cr, Ba, Ni and $^{87}Sr/^{86}Sr_i$, ε^{Nd}, ε^{Hf} suggests that the isotopic enrichment did not result from assimilation of continental crust by a primitive mafic end-member magma. Moreover, the most mafic members display crust-like isotopic signatures, similar to the intermediate members and even to the granites from composite dykes. An alternative interpretation that the lamprophyres are the result of assimilation of Fe-Mg rich crustal

rocks of suitable composition, e.g. the graphitic metapelites of the Parautochthonous Unit (Faure et al., 2001), does not seem viable, as such sediments are unlikely to be sufficiently rich in Cr and Ni. Furthermore, lamprophyres and other high-K–Mg rocks referred to as vaugnerites are ubiquitous in the FMC, where they have intruded several different rock types of the nappe pile (Montel & Weisbrod, 1986; Sabatier, 1991; Couzinié et al., 2016). These other high-K–Mg rocks have chemical and isotopic signatures similar to the lamprophyres reported in this work, pointing to the enriched mantle as the most likely source (Couzinié et al., 2016).

Magmas derived from mantle sources modified by subducted components usually differ from MORBs and OIBs by enrichment in Th and Nb compared to Yb (Pearce, 2008) (Fig. 11a). As is the case for modern sediments (GLObal Subducted Sediments – GLOSS; Plank and Langmuir, 1998), the studied calc-alkaline lamprophyres show jagged spidergrams marked by low Nb–Ta–Ti concentrations and elevated Th, U and Pb. All these geochemical features coupled with low Nb/La ratios, enrichment in LILE, LREE and depletion in HFSE in primitive-mantle-normalized multi-element diagrams suggest that the enriched lithospheric mantle was the most likely source for the lamprophyres. Likewise, the relatively low $^{87}Sr/^{86}Sr_i$ ratios (0.7080– 0.7106) are consistent with recent mantle enrichment, probably during the Silurian–Devonian subduction.

The presence of phlogopite identified in the lamprophyres and also the elevated Rb/Sr and low Ba/Rb ratios strongly indicate that phlogopite was the dominant hydrous phase in the mantle source (Fig. 11b) (e.g., Butvina et al., 2021; Condamine et al., 2022). Moreover, high-K_2O magmas with shoshonitic affinities are a typical product of partial melting of phlogopite-bearing lithospheric mantle that has been metasomatised by fluids or melts derived from the continental crust or marine sediments during subduction (Conceição and Green, 2004; Förster et al., 2019; Prelević et al., 2012). (Fig. 11c).

The $\delta^{18}O_{Qtz}$ values can be used as a proxy for the original magma $\delta^{18}O$ values (e.g., Harris et al., 2005). The parental magma would be about 1‰ lower than $\delta^{18}O_{Qtz}$ values (e.g. Fourie and Harris, 2011). The calc-alkaline lamprophyres display high $\delta^{18}O_{Qtz}$ values ($\delta^{18}O$ = 10.76 to 10.80), suggesting an average $\delta^{18}O$ value of ~ 10‰ for the original magma. This is close to the boundary between I- and S-type granites suggested by Harris et al. (1997) (Fig. 12). The $\delta^{18}O$ values expected for an uncontaminated mantle-derived magma is about 5.7‰ (Eiler, 2001) and fractional crystallization from a primitive magma can at most change $\delta^{18}O$ values by ~1.0‰ for a 20% increase in SiO_2 content (Bindeman, 2008; Bucholz et al., 2017). Either a very high $\delta^{18}O$ contaminant or a very high proportion of crustal assimilation would have been required to raise the $\delta^{18}O$ value from 5.7 to 10‰. Simple mixing calculations between mantle and average of upper continental crust ($\delta^{18}O$ = 15‰) show that ~ 50% of crustal assimilation would be necessary to raise $\delta^{18}O$ values above 10‰ (Fig. 13). This high degree of crustal assimilation is inconsistent with the high compatible element contents and the relatively low $^{87}Sr/^{86}Sr_i$ ratios of the lamprophyres which point to little or no crustal assimilation being involved in the origin of lamprophyres. Therefore, we suggest that the high $\delta^{18}O$ values in lamprophyres result from contamination with high $\delta^{18}O$ material already in the mantle source.

High $\delta^{18}O$ values are common in sedimentary rocks. Oceanic carbonate-bearing sediments have $\delta^{18}O$ values of 25 to 32‰ and pelagic clays from 15 to 25‰ (Eiler, 2001). Values from the silicate upper continental crust are around 10 and 20‰ (Taylor and Shepard, 1986). Extremely high $\delta^{18}O$ values have been reported in peraluminous granite in ophiolite as a product of the melting of subducted pelagic sediments, leading to magma $\delta^{18}O$ values above 20‰ (Spencer et al., 2017) (Fig. 12). In this work, the high $\delta^{18}O$ values from lamprophyres (> 10‰) indicate that

453 the crustal component that metasomatised the mantle source was dominated by sedimentary
454 material.

455 To quantify the nature of the mantle source, mixing calculations using Sr, Nd and O isotopic
456 systems were applied. Simple mixing calculations between mantle and potential contaminants
457 indicate that ~ 20% of oceanic carbonate-bearing sediment ($\delta^{18}O$ = 28‰) or ~ 35% of pelagic
458 clay ($\delta^{18}O$ = 20‰) would be necessary to increase $\delta^{18}O$ values to > 10‰ (Fig. 13).

459 Following the same approach, simple magma mixing calculations using $^{87}Sr/^{86}Sr_i$ and ε^{Nd}
460 from the Variscan mantle and sedimentary material were applied. A proxy for the original,
461 subduction-modified depleted Variscan mantle can be derived from Devonian arc-related
462 magmatism and ophiolites of the Variscan Belt. Arc magmatism, resulting from fluid-fluxed
463 melting of the mantle wedge should have ε^{Nd} close to the canonical depleted mantle values but
464 $^{87}Sr/^{86}Sr$ offset to higher values (e.g., Bouilhol et al., 2013). The Devonian rocks of Massif
465 Central have ε^{Nd} up to +7 (Pin and Paquette, 2002). They also have $^{87}Sr/^{86}Sr$ ratios that are
466 invariably higher than the expected value of 0.703 on the "mantle array" for rocks with ε^{Nd} = +7,
467 as expected for arc magmas and likley reflecting some continental crustal component.
468 Consequently, we estimate the Variscan mantle composition at that time to be ε^{Nd} = +7, $^{87}Sr/^{86}Sr$
469 = 0.703.

470 In the case of FMC, the pre-Variscan metasediments are compositionally close to sediments
471 from the former northern Gondwana margin (Chelle-Michou et al., 2017; Couzinié et al., 2017).
472 We modelled binary mixing with several end-members, covering the range of Variscan
473 metasediments (Solgadi et al., 2007; Williamson et al., 1992) and GLOSS (Plank and Langmuir,
474 1998). Mixing calculations indicate that the amount of sedimentary material mixed with mantle

475 required to model the crustal isotopic signatures in Sr–Nd isotopic systems is 25–40% (Fig. 14a),
476 depending on the composition of the sediment end-member.

477 Lu–Hf and Sm–Nd isotopic systems display similar behavior during most magmatic
478 processes and the composition of mantle and crust are correlated, evolving in a "mantle array"
479 trend (Chauvel et al., 2008). Subchondritic whole-rock ε^{Nd} and ε^{Hf} imply mantle enrichment with
480 crustal materials.

481 The textural evidence from the lamprophyres and granites argues for the involvement of a
482 carbonate component in the magmas and the existence of an immiscible carbonate liquid in the
483 lamprohyres during crystallization. Ocellar carbonates are commonly described as the products of
484 immiscibility between silicate and carbonate liquids in potassic, alkaline, mantle-derived igneous
485 rocks (e.g., Huang et al., 2002 and references therein). The presence of carbonates in
486 lamprophyre might indicate that the crustal component was a carbonate-bearing sediment. This
487 composition corroborates the high oxygen fugacity identified in the mantle beneath FMC, which
488 is attributed to the addition of volatiles, including CO_2, in the mantle during Variscan subduction,
489 triggering CO_2, H_2O and K metasomatism (Martin et al., 2017).

490 After inferring the probable nature of the contaminant, the partial melting mechanism that
491 generated the lamprophyres was investigated. Non-modal partial melting models of a calculated
492 source with 65–80% of DM and 20–35% of a contaminant (GLOSS composition) show that
493 melts produced by 10 to 20% partial melting match the trace-element composition of
494 lamprophyres and associated granites (Fig. 15a, b). This model resembles results of experimental
495 melting of metasomatised mantle by Condamine et al. (2022).

496 The high HREE contents are consistent with shallow melting of a spinel peridotite, i.e., in the
497 absence of garnet. Lamprophyres and granites display higher LREE contents than the modelling

predicts, suggesting a pelagic clay richer in Rb and Ba than the average global sediments used in the calculation (Plank and Langmuir, 1998), or melts derived from sediments, more enriched in LREE than GLOSS.

In summary, the evidence from this study indicates that the magmas that produced the lamprophyric component of the composite dykes was produced by 10–20% melting of a metasomatised mantle source in the spinel-lherzolite field. This CO_2-, H_2O-, K-enriched metasomatised mantle was phlogopite-bearing and resulted from reaction with sediment-derived melts or fluids that were probably introduced into the mantle during Silurian–Devonian subduction.

5.2.2 Origin of granites

The studied dykes are composite and include lamprophyric and granitic components, which display field evidence indicating that they coexisted. They are also characterized by very similar geochemical features. Thus, the lamprophyres and granites of the composite dykes were comagmatic and show a mixture of "crust-like" and "mantle-like" geochemical features. Three main hypotheses or combinations thereof are plausible for the origin of the granites:

1. The lamprophyres and the granites are related by differentiation processes, such as fractional crystallization, although remelting of underplated lamprophyres to produce the granites would result in broadly the same patterns;
2. The lamprophyres and the granites represent distinct magmas, an enriched-mantle derived magma for the lamprophyres and a crust-derived magma for the granites, that mingled and mixed;
3. The granite and the lamprophyres are both direct products of melting of the enriched mantle source but reflect different degrees of partial melting. This could be achieved by

different source compositions, different temperatures of partial melting, different volatile contents (more CO_2 in the lamprophyre source), or some combination.

We briefly discuss each hypothesis below.

The granites in the dykes share many geochemical characteristics with the lamprophyres, including nearly identical isotopic ratios and trace-element concentrations. However, the granites and the lamprophyres are not connected by differentiation trends, as illustrated by the fact that the lamprophyres are richer in most incompatible elements than the granites. This enrichment is inconsistent with a simple model of fractional crystallization of mafic into felsic magmas and is also inconsistent with the granites being the product of partial melting of the lamprophyres.

Major elements such as K_2O, Na_2O and Al_2O_3 are relatively constant with increasing SiO_2 content, implying no significant fractionation of K-feldspar, plagioclase and biotite in high-K magmas (e.g., Wang et al., 2021) (Fig. 6a, b, c). The increase in volume and size of phenocrysts of K-feldspar in the granitic component demonstrate that a considerable decrease in K_2O is expected during fractional crystallisation. Furthermore, a fractionation process involving plagioclase would display similar behavior for CaO and Sr on the binary plots against SiO_2 in Figure 6 display distinct behavior from CaO and Sr against SiO_2 contents, demonstrating that fractional crystallization from the lamprophyres is unlikely to generate the granites.

In general, fractional crystallization involving clinopyroxene would remove compatible elements such as Cr and Ni. The high Cr (30–140 ppm; 80.9 on average and in cases over 100 ppm in granite with SiO_2 = 70 wt%) and Ni (14–40 ppm; 24.4 on average) content in the granites are inconsistent with fractional crystallisation of clinopyroxene playing an important role in the formation of granites. Moreover, no cumulate textures are observed in lamprophyres and no pyroxenites are described in the area. Therefore, this fractionation model is unlikely.

544 Cogenetic granite may result from mixing between lamprophyric and crust-derived magmas
545 at crustal conditions. Petrological evidence favoring this model consists of the presence in ca.
546 10% of zircon xenocrysts in granites from composite dykes and the existence of corroded quartz
547 xenocrysts mantled by carbonate and amphibole in lamprophyres. Quartz xenocrysts rimmed by
548 amphibole and carbonate are interpreted as typical magma-mixing texture (e.g., Janoušek et al.,
549 2004). In this way, we consider that assimilation of a crustal component is involved in the
550 petrogenesis of the granites from the composite dykes.
551 Linear trends observed in many (but not all) binary chemical plots between lamprophyre and
552 granite might indicate magma mixing between these two end members. However, similar trends
553 are observed in fractional crystallization or partial melting processes (Janoušek et al., 2016).
554 Radiogenic isotopes are generally not fractionated during partial melting or fractional
555 crystallization/accumulation and, therefore, are the best tools for deciphering open-system
556 processes such as magma mixing (e.g., Sun et al., 2010).
557 Large variations in zircon ε^{Hf} in granitic rocks have been attributed to magma mixing
558 between crustal and mantle-derived magmas (Griffin et al., 2002; Storck et al., 2021; Yang et al.,
559 2007) or inheritance of heterogeneities in detrital zircon record from the sedimentary source of
560 anatectic granites (e.g., Villaros et al., 2012).
561 In the present study, zircon ε^{Hf} values from lamprophyres and granites vary from –7.8 to
562 +0.4 with more than 90% of the data falling between –5.0 and –1.6, i.e. within less than 4 ε^{Hf}
563 units. This is a limited variation with respect the analytical uncertainty (*c.* ± 1.5 on average). In
564 the case of mixing of magmas with typical mantle and crustal Hf isotopic compositions, a
565 substantially wider range in ε^{Hf} values is expected (up to 10 ε^{Hf} units). Also, crustal and mantle
566 signatures would be more prominent, i.e., mantle component migrating towards positive and

crustal component towards negative ε^{Hf} values (e.g., Storck et al., 2021). Likewise, magmatic rims mantling an old inherited core display different Hf isotopic signatures than cores, which indicates that the inheritance does not control the isotopic composition of the magmatic rim. The ε^{Hf} values from lamprophyres and granites are similar and overlap, suggesting that mixing within different and contrasting magmas did not play an important role.

In terms of oxygen isotopes, the lack of correlation between $\delta^{18}O$ values and $^{87}Sr/^{86}Sr_i$, ε^{Nd} and ε^{Hf} renders the slight correlation between SiO_2 and Cr or Ni meaningless. Therefore, the small difference in $\delta^{18}O$ values between lamprophyres and granites (less than 0.5‰) is consistent with source-related variation or homogenization of the magma than mixing between two different and contrasting magmas.

Although crustal melts are regionally widespread in FMC, the ASGL Pluton lacks obviously crustally-derived granites, such as strongly peraluminous cordierite- or muscovite-bearing granites that are ubiquitous elsewhere in the FMC. In addition, the lack of well-defined mixing trends for major elements, trace elements and isotopes suggests that magma mixing was not a dominant process. Therefore, we favor only local and limited assimilation.

The comagmatic nature of the lamprophyres and granites, as well as their very similar isotopic signatures, indicates that a third hypothesis needs to be evaluated: That the granites and lamprophyres were both produced by directly by partial melting of metasomatised mantle. Mantle peridotite or lherzolite metasomatised by either subducted metasediment or melts derived from such metasedimentsis widely accepted to be the source of post-collisional K-rich magmatism (e.g. Förster et al., 2019, 2020, 2021; Mallik et al., 2015). More specifically, recent studies reported that mixing between peridotite and sediment may produce rocks that are likely to be

quartz normative (Förster et al., 2020, 2021) with major- and trace-element patterns similar to those in the Aigoual dykes.

The available data clearly rule out the possibility that the granites formed by fractional crystallization of a lamprophyric parent magma. It is also very unlikely that the granites formed predominantly from a crustally derived magma because the granites have typical SiO_2 contents, yet are strongly enriched in mantelitic elements. They also have isotopic compositions that are very similar to the lamprophyres. The ages of the inherited zircon crystals in the granites do indicate some assimilation of Variscan basement, but the range of ε^{Hf} values (approximately -8 to +4) for these zircons relative to ε^{Hf} in the magmatic zircons (90% between approximately -5 and -2) clearly indicates that this Variscan basement was not a major source of magma to the granites. The data are consistent with the granite magma forming via the partial melting of a mantle source metasomatised in the manner defined, with a minor amount of assimilation of Variscan crust to explain the inherited zircons. As the granite and lamprophyre magmas are isotopically very similar at source, the major and trace element arrays defined by the granitic and lamprophyric components may be shaped by mixing between these magmas that is invisible from an isotopic perspective.

5.2.3 Texture of the microgranites

The preservation of the studied composite dykes and the fine-grained, quench textures in the granites may be a direct consequence of the presence of carbonate in the system. The absence of clinopyroxene in the lamprophyres and its presence in the granites may be explained by the textural association of biotite/phlogopite with carbonate pseudomorphing a prior mafic mineral in the lamprophyres. This reaction replacing clinopyroxene and/or olivine can be explained as a response to increasing aCO_2 and aH_2O in the lamprophyric magma during crystallization (Blank

612 and Brooker, 1994; Solomatova et al., 2020). As the presence of carbonate facilitates partial
613 melting of the mantle (e.g., Dasgupta et al., 2013), carbonated portions of the metasomatised
614 mantle source are inferred to have melted preferentially to produce the lamprophyres.
615 The CO_2 plays a fundamentally different role in the melting of mantle and crustal rocks and
616 its solubility is strongly dependent of pressure, melt composition, particularly SiO_2 content
617 (Blank and Brooker, 1994; Ni and Keppler, 2013). During melting of mafic and ultramafic rocks
618 at mantle pressures, the solubility of CO_2 increases with increasing pressure and decreasing SiO_2
619 contents (Brooker et al., 2001). CO_2 has a very low solubility in felsic melts at crustal pressures,
620 whilst H_2O solubility is high, consistent with the powerful effect of H_2O in depressing the granite
621 solidus (Blank and Brooker, 1994; Brooker et al., 2001). The consequence of CO_2 being present
622 in these systems is to raise the solidus temperature by lowering the water activity (Scaillet et al.,
623 1997). Therefore, CO_2-fluids derived from cooling mantle-derived magmas that intruded the crust
624 may limit the possibilities for complete mixing between the mafic and felsic magma at shallow
625 levels. Our study potentially records an example of this behavior, in which the mantle-derived
626 lamprophyre magmas quenched the granitic magmas with which they mingled, once carbonate
627 saturation of the mafic magma occurred.

628 **5.3 Implications for crustal growth**

629 In any magmatic episode, the ratio of new mantle-derived magma relative to that derived
630 from the partial melting of older crustal material, determines the amount of crustal growth
631 achieved. In the case of the FMC, a large proportion of the magmatic rocks (MPG, CPG and
632 Velay migmatites) were derived from melting of local crust. Therefore, these rocks did not
633 contribute to crustal growth and corresponded to pure crustal recycling (e.g. Moyen et al., 2017).
634 On the other hand, vaugnerite and the KCG granites contain a contribution of mantle-derived

635 material and thus, to some degree, represent the formation of new continental crust (Couzinié et
636 al., 2016; Moyen et al., 2017). Couzinié et al. (2016) has demonstrated that Hf–O isotopes in
637 zircon in this case do not identify additions of new mantle-derived material to the crust.
638 Therefore, the process of crustal growth may be underestimated throughout geological time, since
639 many studies were carried out relying on the zircon record (e.g., Belousova et al., 2010;
640 Hawkesworth and Kemp, 2006).
641 This study has illuminated the reasons for this, clearly mantle derived magmas such as the
642 vaugnerites in this study, are derived from mantle source rocks with sufficient degrees of
643 metasomatism by a subducted crustal component that conventional radiogenic isotopic systems,
644 such as Rb–Sr, Sm–Nd and Lu–Hf, as well as O isotope ratios, attain values consistent with their
645 derivation from the continental crust. The high $\delta^{18}O$ of clay-rich sediments and the low
646 abundance the relevant radiogenic precursor isotopes in the mantle, result in a relatively small
647 proportion of sediment-rich crustal material (< 30%) recycled into the mantle being sufficient to
648 control all incompatible elements contents and form the "crust-like" isotopic signature observed
649 in mafic post-collisional magmatism (Couzinié et al., 2016; Jacob et al., 2021). However, in
650 detail, the calculated mantle:crust ratio may be dependent on the element, or isotopic system
651 used, as well as the exact composition of deep crustal contaminant and the mechanism of
652 metasomatism (Couzinié et al., 2016; Janoušek et al., 2020; 2021).
653 Our results demonstrate that between 20 and 35% of the budget of Sr, Nd, Hf and other
654 incompatible elements comes from the crust and therefore does not constitute additions of new
655 material. However, at the same time, the budget of compatible elements such as Mg, Fe, Ni, Cr is
656 strongly controlled by the mantle component and represents addition of new material to the crust.
657 In the lamprophyres, the mafic character and dual geochemical signature displays mantle and

crustal contributions. Even though the mantle contribution is hidden from an isotopic point of view, between 65 to 80% of material comes from the mantle. In the case of the Aigoual composite dykes, this broad finding applies to modelled mantle crust ratios constrained on the basis of radiogenic isotope rations, trace element compositions and oxygen isotope ratios (Fig. 13, 14 and 15).

Although less evident, the same process occurs in the granites of composite dykes. Assimilation of a minor amount of crustal material is likely be involved in their petrogenesis, but the relatively high Cr, Ni, also FeO, and MgO contents in relation to purely crustaly-derived granites in the FMC reflects the mantle component involved in their genesis. The intimate relation (physically and geochemically) between lamprophyre and granite described in this work from the composite dykes at northern border of the Aigoual granite provides constraints on the mantle contribution in post-collisional granitoids from the FMC. The fact that the chemistry of the Aigoual granite lies at the mafic end of the trend defined by the granites from the composite dykes, as well as the common occurrence of rounded lamprophyric enclaves in the granite, suggests that it formed by mixing with approximately the same amount of lamprophric magma as the most mafic granites in the composite dykes.

High-K–Mg mafic rocks are low in volume in the FMC, forming ~ 10% outcrops, and therefore their contribution to crustal growth may be relatively minor. However, the findings of this study demonstrate a significant fraction of mantle material in the granites of the composite dykes, in the Aigoual granite and, thus, likely also in other KCG granites in the FMC (ca. 25% of outcrop area). Considering that between 65% and 80% of the material from lamprophyres and KGC granites came from the mantle and both represent < 35% of granitoids outcrops in the FMC, approximately 22 to 28% of the magmatic material represented by the KGC likely came

from the mantle and, despite the crustal-like incompatible element contents and isotopic signatures, represents a substantial new addition to the crust.

6. Conclusions

In summary, lamprophyric-granitic composite dykes from the northern border of the Aigoual granite (southeastern Massif Central, France) record interaction between the mantle and crust in the source of the magmas. The intrusion of these magmas into the late/post-orogenic continental crust represents significant long-term additions of new crust with excellent potential for preservation. Their intrusion was coeval with the emplacement of Aigoual granite between 311 and 313 Ma, which shares their source but underwent more complete homogenization because the magmas that formed the granite did not freeze in their conduits. Crystallization of the granitic component of the composite dykes in the conduits was likely a consequence CO_2-saturation of the lamprophyric component and consequent quenching of the granite portion. Lamprophyres display crust-like signatures in their Sr, Nd, Hf, O isotopes and other incompatible elements, and were the product of 10–20% of partial melting from metasomatised mantle. This mantle can be modelled by mixing between 20 and 35% of sediments from northern Gondwana margin with 65 to 80% of depleted mantle. The melting processes occurred at shallow depths in the spinel stability field. Granites have a mantle-derived component, evident from their high Cr, Ni, FeO and MgO contents compared with typical anatectic granites in the FMC. In terms of crustal growth, the results imply that between 22 and 28% of magmatic material in the FMC was mantle-derived. This study demonstrates that, although hidden by crustal signatures in terms of radiogenic isotopes and incompatible elements, the mantle contribution in post-collisional magmatism can be significant. Considering their greater preservation potential throughout

geological time, post-collisional sites represent a meaningful contributor to long-term crustal growth.

Acknowledgements

This research was supported by RSA NRF grant to Gary Stevens via the SARChI program and by IRP BuCoMo, a collaborative research project funded by the CNRS and the NRF. This is BuCoMo contribution A15. We thank Llelani Coetzer for sample preparation; Riana Rossouw for LA-SF-ICP-MS analyses; Madelaine Frazenburg and Alicia Botes for the help with remote SEM analyses in 2020; Fayrooza Rawoot and Petrus Le Roux for assistance with Sr, Nd and Hf isotope measurements; and, Sherissa Roopnarain for help with the O-isotope analyses. We thank Vojtech Janoušek for a very thorough and constructive review of the manuscript.

7. References

Abdel, A.F.M.R., Nassar, P.E., 2004. Cenozoic volcanism in the Middle East: Petrogenesis of alkali basalts from northern Lebanon. Geological Magazine 141, 545-563.

Barbarin, B., 1999. A review of the relationships between granitoid types, their origins and their geodynamic environments. Lithos, 46: 605-626.

Becker, H., Wenzel, T., Volker, F., 1999. Geochemistry of glimmerite veins in peridotites from Lower Austria – implications for the origin of K-rich magmas in collision zones. Journal of Petrology 40, 315–338.

723 Belousova, E.A., Kostitsyn, Y.A., Griffin, W.L., Begg, G.C., O'Reilly, S.Y., Pearson, N.J., 2010.
724 The growth of the continental crust: Constrains form zircon Hf-isotope data. Lithos 119, 457-466.

725 Bindeman, I., 2008. Oxygen isotopes in mantle and crustal magmas as revealed by single crystal
726 analysis. In: Purtika, K.D., Tepley III, F.J. (eds) Minerals, Inclusions and Volcanic processes.
727 Reviews in Mineralogy and Geochemistry 69, 445-478.

728 Blank, J.G., and Brooker, R.A., 1994. Experimental studies of carbon dioxide in silicate melts:
729 Solubility, speciation, and stable carbon isotope behavior. In: Carroll, M.R., Holloway, J.R.
730 (Eds.), Volatiles in Magmas. Reviews in Mineralogy and Geochemistry, 30, 157-186.

731 Bonin, B., 2004. Do coeval mafic and felsic magmas in post-collisional to within-plate regimes
732 necessarily imply two contrasting, mantle and crustal, sources? A review. Lithos 78, 1-24.

733 Bouilhol, P., Jagoutz, O., Hanchar, J.M., Dudas, F.O., 2013. Dating the India–Eurasia collision
734 through arc magmatic records. Earth and Planetary Science Letters 366, 163-175.

735 Brichau, S., Respaut, J.P., Monié, P., 2008. New age constraints on emplacement of the Cévenol
736 granitoids, South French Massif Central. International Journal of Earth Science 97, 725–738.

737 Brooker, R.A., Kohn, S.C., Holloway, J.R., McMillan, P.F., 2001. Structural controls on the
738 solubility of CO_2 in silicate melts: Part I: bulk solubility data. Chemical Geology 174, 225-239.

739 Bucholz, C.E., Jagoutz, O., VanTongeren, J.A., Setera, J., Wang, Z., 2017. Oxygen isotope
740 trajectories of crystallizing melts: Insight from modelling and the plutonic record. Geochimica et
741 Cosmochimica Acta 207, 154-184.

742 Butvina, V.,G., Safonov, O.G., Vorobey, S.S., Limanov, E.V., Kosova, S.A., Van, K.V.,
743 Bondarenko, G.V., Garanin, V.K., 2021. Experimental study of reactions forming phlogopite and
744 potassic titanates as mineral indicators of metasomatism in the upper mantle. Geochemistry
745 International 59, 757-777.

746 Chantraine, J., Autran, A., Cavelier, C., 1996. Carte géologique de la France à l'échelle du
747 millionième (6e édition), BRGM, Orléans.

748 Chauvel, C., Lewin, E., Carpentier, M., Arndt, N., Marini, J-C., 2008. Role of recycled oceanic
749 basalt and sediment in generating the Hf–Nd mantle array. Nature Geoscience 1, 64–67.

750 Chelle-Michou, C., Laurent, O., Moyen, J-F., Block, S., Paquette, J-L., Couzinié, S., Gardien,
751 V., Vanderhaeghe, O., Villaros, A., Zeh, A., 2017. Pre-Cadomian to late-Variscan odyssey of the
752 eastern Massif Central, France: Formation of the West European crust in a nutshell. Gondwana
753 Research 46, 170-190.Conceição, R. V., Green, D. H., 2004. Derivation of potassic (shoshonitic)
754 magmas by decompression melting of phlogopite+pargasite lherzolite. Lithos 72, 209-229.

755 Couzinié, S., Laurent, O., Poujol, M., Mintrone, M., Chelle-Michou. C., Moyen, J-F., Bouilhol, P.,
756 Vezinet, A., Marco, L., 2017.Cadomian S-type granites as basement rocks of the Variscan belt
757 (Massif Central, France): Implications for the crustal evolution of the north Gondwana margin.
758 Lithos 286, 16-34.

759 Chiba, H., Chacko, T., Clayton, R.N., Goldsmith, J.R., 1989. Oxygen isotope fractionations
760 involving diopside, forsterite, magnetite, and calcite: applications to geothermometry. Geochim
761 Cosmochim Acta 53, 2985–2995.

762 Clemens, J.D., Darbyshire, D.P.F., Flinders, J., 2009. Sources of post-orogenic calc-alkaline
763 magmas: the Arrochar and Garabal Hill–Glen Fyne complexes, Scotland. Lithos 112, 524–542.

764 Clemens, J.D., Stevens, G., Mayne, J.M., 2021. Do arc silicic magmas form by fluid-fluxed
765 melting of older arc crust or fractionation of basaltic magmas? Contributions to Mineralogy and
766 Petrology 176, 44.

767 Condamine, P., Médard, E., 2014. Experimental melting of phlogopite-bearing mantle at 1 GPa:
768 Implications for potassic magmatism. Earth and Planetary Science Letters 397, 80-92.

769 Condamine, P., Couzinié, S., Fabbrizio, A., Devidal, J.L., Médard, E., 2022. Trace element
770 partitioning during incipient melting of phlogopite-peridotite in the spinel and garnet stability
771 fields. Geochimica et Cosmochimica Acta 327, 53-78.

772 Condie, K.C., 2014. Growth of continental crust: a balance between preservation and recycling.
773 Mineralogical Magazine 78, 623-637.

774 Couzinié, S., Moyen, J-F., Villaros, A., Marignac, C., 2014. Temporal relationships between
775 Mg–K mafic magmatism and catastrophic melting of the Variscan crust in the southern part of
776 the Velay Complex (Massif Central, France). Journal of Geosciences 59, 69-86.

777 Couzinié, S., Laurent, O., Moyen, J.F., Zeh, A., Bouilhol, P., Villaros, A., 2016. Post-collisional
778 magmatism: Crustal growth not identified by zircon Hf–O isotopes. Earth and Planetary Science
779 Letters 456, 182-195.

780 Couzinié, S., Laurent, O., Chelle-Michou, C., Bouilhol, P., Paquette, J.L., Gannoun, A.M.,
781 Moyen, J.F., 2019. Detrital zircon U–Pb–Hf systematics of Ediacaran metasediments from the

French Massif Central: Consequences for the crustal evolution of the north Gondwana margin. Precambrian Research 324, 269-284.

Dasgupta, R., 2013. Ingassing, storage, and outgassing of terrestrial carbon though geologic Time. In: Hazen, R.M., Jones, A.P., Baross, J.A., (eds) Carbon in Earth. Reviews in Mineralogy and Geochemistry 75, 183-229.

Davies, J.H., von Blanckenburg, F., 1995. Slab breakoff: a model of lithosphere detachment and its test in the magmatism and deformation of collisional orogens. Earth and Planetary Science Letters 129, 85-102.

Dhuime, B., Hawkesworth, C.J., Cawood, P. 2011. When continents formed. Science 331, 154–155.

Downes, H., Shaw, A., Williamson, B.J., Thirlwall, M.F., 1997. Sr, Nd and Pb isotope geochemistry of the Hercynian granodiorites and monzogranites, Massif Central, France. Chemical Geology 136, 99–122.

Eiler, J.M., 2001. Oxygen isotope variations of basaltic lavas and upper mantle rocks. In: Valley, J.W., Cole, D.R., (eds) Stable Isotope Geochemistry. Reviews in Mineralogy and Geochemistry 43, 319–364.

Ewing, R.C., Meldrum, A., Wang, L.M., Weber, W.J., Corrales, R.J., 2003. Radiation effects in zircon. In: Hanchar, J.M., Hoskin, P.W.O., (eds) Zircon. Reviews in Mineralogy and Geochemistry 53, 387-485.

Faure, F., Charonnat, X., Chauvet, A., 1999. Schéma structural et évolution tectonique du domaine para-autochtone cévenol de la chaîne hercynienne (Massif central français). Comptes Rendus de l'Académie de Sciences 328, 401-407.

Faure, M., Charonnat, X., Chauvet, A., Chen, Y., Talbot, J-Y., Martelet, G., Courrioux, G., Monie, P., Milesi, J-P., 2001. Tectonic evolution of the Cevennes para-autochthonous domain of the Hercynian French Massif Central and its bearing on ore deposits formation. Bulletin de la Société Géologique de France 172, 687–696.

Faure, M., Lardeaux, J.M., Ledru, P., 2009. A review of the pre-Permian geology of the Variscan French Massif Central. Comptes Rendus Geoscience 341, 202-213.

Förster, M.W., Prelević, D., Buhre, S., Mertz-Kraus, R., Foley, S.F., 2019. An experimental study of the role of partial melts of sediments *versus* mantle melts in the sources of potassic magmatism. Journal of Asian Earth Sciences 177, 76–88.

Förster, M.W., Buhre, S., Xu, B., Prelević, D., Mertz-Kraus, R., Foley, S.F., 2020. Two-stage origin of K-enrichment in ultrapotassic magmatism simulated by melting of experimentally metasomatized mantle. Minerals 10, 41. https://doi.org/10.3390/min10010041.

Förster, M.W., Bussweiler, Y., Prelević, D., Daczko, N.R., Buhre, S., Mertz-Kraus, R., Foley, S.F., 2021. Sediment–peridotite reaction controls fore-arc metasomatism and arc magma geochemical signature. Geosciences, 11, 372. https://doi.org/10.3390/geosciences11090372.

Fowler, M.B., Henney, P.J., 1996. Mixed Caledonian appinite magmas: implications for lamprophyre fractionation and high Ba–Sr granite genesis. Contributions to Mineralogy and Petrology 126, 199-215.

822 Fourie, D.S., Harris, C., 2011. O-isotope Study of the Bushveld Complex Granites and
823 Granophyres: Constraints on Source Composition, and Assimilation. Journal of Petrology 52,
824 2221–2242.

825 Furman, T., Graham, D., 1999, Erosion of lithospheric mantle beneath the East African Rift
826 system: geochemical evidence from the Kivu volcanic province. Lithos 48, 237–262.

827 Griffin, W.L., Wang, X., Jackson, S.E., Pearson, N.J., O'Reilly, S.Y., Xu, X., Zhou, X., 2002.
828 Zircon chemistry and magma mixing, SE China: In-situ analysis of Hf isotopes, Tonglu and
829 Pingtan igneous complexes. Lithos 61, 237–269.

830 Griffin, W.L., Belousova, E.A., Shee, S.R., Pearson, N.J., O'Reilly, S.Y., 2004. Archean crustal
831 evolution in the northern Yilgarn Craton: U–Pb and Hf-isotope evidence from detrital zircons.
832 Precambrian Research 131, 231-282.

833 Harris, C., Faure, K., Diamond, R.E., Scheepers, R., 1997. Oxygen and hydrogen isotope
834 geochemistry of S- and I-type granitoids: the Cape Granite suite, South Africa. Chemical
835 Geology 143, 95–114.

836 Harris, C., Pronost, J.J.M., Ashwal, L.D., Cawthorn, R.G., 2005. Oxygen and hydrogen isotope
837 stratigraphy of the Rustenburg Layered Suite, Bushveld Complex: constraints on crustal
838 contamination. Journal of Petrology 46, 579-601.

839 Hawkesworth, C.J., and Kemp, A.I.S., 2006. Using hafnium and oxygen isotopes in zircons to
840 unravel the record of crustal evolution. Chemical Geology 226, 144-162.

841 Hawkesworth, C., Cawood, P., Kemp, T., Storey, C., Dhuime, B., 2009. A matter of preservation.
842 Science, 323, 49-50.

843 Hofmann, A., 1988.
844

845 Huang, Z., Liu, C., Xiao, H., Han, R., Xu, C., Li, W., Zhong, W., 2002. Study on the carbonate
846 ocelli-bearing lamprophyre dykes in the Ailaoshan gold deposit zone, Yunnan Province. Science
847 in China Series D: Earth Sciences 45, 494 https://doi.org/10.1360/02yd9051.

848 Jacob, J.B., Moyen, J.F., Fiannacca, P., Laurent, O., Bachmann, O., Janoušek, V., Farina, F.,
849 Villaros, A., 2021. Crustal melting vs. fractionation of basaltic magmas: Part 2, attempting to
850 quantify mantle and crustal contributions in granitoids. Lithos 402-403, 106292.

851 Janoušek, V., Braithwaite, C.J.R., Bowes, D.R., Gerdes, A., 2004. Magma-mixing in the genesis
852 of Hercynian calc-alkaline granitoids: an integrated petrographic and geochemical study of the
853 Sázava intrusion, Central Bohemian Pluton, Czech Republic. Lithos 78, 67-99.

854 Janoušek, V., Holub, F.V., 2007. The causal link between HP–HT metamorphism and ultrapotassic
855 magmatism in collisional orogens: case study from the Moldanubian Zone of the Bohemian Massif.
856 Proceedings of the Geologists' Association 118, 75–86.

857 Janoušek, V., Moyen, J.F., Martin, H., Erban, V., Farrow, C., 2016. Geochemical Modelling of
858 Igneous Processes—Principles and Recipes in R Language. Bringing the Power of R to a
859 Geochemical Community. Springer-Verlag, Berlin, Heidelberg.

860 Janoušek, V., Hanžl, P., Svojtka, M., Hora, J.M., Erban Kochergina, Y.V., Gadas, P., Holub, F.V.,
861 Gerdes, A., Verner, K., Hrdličková, K., Daly, J.S., Buriánek, D., 2020. Ultrapotassic magmatism
862 in the heyday of the Variscan Orogeny - the story of the Třebíč Pluton, the largest durbachitic body
863 in the Bohemian Massif. International Journal of Earth Sciences 109, 1767–1810.

864 Janoušek, V., Hora, J.M., Erban Kočergina, J.V., Magna, T., Tabaud, A.S., Andronikov, A.,
865 Couzinié, S., Holub, F.V., 2021. Cryptic crustal growth in European Variscan Orogen: evidence
866 from ultrapotassic plutonic rocks of the Bohemian Massif. In: Gregáňová, M., Molčan Matejová,
867 M., Šimonová, V. (eds) 18th Meeting of the Central European Tectonic Groups, 25th Meeting of
868 the Czech Tectonic Studies Group, Terchová – Vrátna, 22-25 September, 2021. Bratislava:
869 Comenius University, 51–52.

870 Kay, R.W. and Kay, S.M., 1993. Delamination and delamination magmatism. Tectonophysics,
871 219: 177-189.

872 Kröner, U., and Romer, R.L., 2013. Two plates – many subduction zones: The Variscan orogeny
873 reconsidered. Gondwana Research 24, 298-329.

874 Lardeaux, J.M., Schulmann, K., Faure, M., Janoušek, V., Lexa, O., Skrzypek, E., Edel, J.B.,
875 Štípská, P. 2014. The Moldanubian Zone in the French Massif Central, Vosges/Schwarzwald and
876 Bohemian Massif revisited: differences and similarities. Geological Society, London, Special
877 Publications 405, 7 – 44.

878 Laurent, O., 2012. Les changements géodynamiques à la transition Archéen–Protérozoïque: étude
879 des granitoïdes de la marge Nord du craton du Kaapvaal (Afrique du Sud). PhD thesis, Université
880 Blaise Pascal, Clermont-Ferrand.

881 Laurent, O., Couzinié, S., Zeh, A., Vanderhaeghe, O., Moyen, J.F., Villaros, A., Gardien, V.,
882 Chelle-Michou, C., 2017. Protracted, coeval crust and mantle melting during Variscan
883 late-orogenic evolution: U–Pb dating in the eastern French Massif Central. International Journal
884 of Earth Science 106, 421–451.

885 Le Maitre, R.W., Streckeisen, A., Zanettin, B., Le Bas, M.J., Bonin, B., Bateman, P., Bellieni, G.,
886 Dudek, A., Efremova, S., Keller, J., Lamere, J., Sabine, P.A., Schmid, R., Sorensen, H., Woolley,
887 A.R., 2002. Igneous Rocks: A Classification and Glossary of Terms, Recommendations of the
888 International Union of Geological Sciences, Subcommission of the Systematics of Igneous
889 Rocks. Cambridge University Press.

890 Lexa, O., Schulmann, K., Janoušek, V., Štípská, P., Guy, A. & Racek, M., 2011. Heat sources
891 and trigger mechanisms of exhumation of HP granulites in Variscan orogenic root. Journal of
892 Metamorphic Geology 29, 79–102.

893 Mallik, A., Nelson, J., Dasgupta, R., 2015. Partial melting of fertile peridotite fluxed by hydrous
894 rhyolitic melt at 2–3 GPa: Implications for mantle wedge hybridization by sediment melt and
895 generation of ultrapotassic magmas in convergent margins. Contributions to Mineralogy and
896 Petrology 168, 48.

897 Martin, A.M., Médard, E., Righter, K., Lanzirotti, A., 2017. Intraplate mantle oxidation by
898 volatile rich silicic magmas. Lithos 292-293, 320-333.

899 Matte, P., 2001. The Variscan collage and orogeny (480–290 Ma) and the tectonic definition of
900 the Armorica microplate: a review. Terra Nova 13, 122-128.

McDonough, W.F., and Sun, S.S., 1995. The composition of Earth. Chemical Geology 120, 223-253.

Melleton, J., Cocherie, A., Faure, M., Rossi, P., 2010. Precambrian protoliths and Early Paleozoic magmatism in the French Massif Central: U–Pb data and the North Gondwana connection in the west European Variscan belt. Gondwana Research 17, 13-25.

Moyen, J.F., Laurent, O., Chelle-Michou, C., Couzinié, S., Vanderhaeghe, O., Zeh. A, Villaros, S., Gardien, V., 2017. Collision vs. subduction-related magmatism: Two contrasting ways of granite formation and implications for crustal growth. Lithos 277, 154-177.

Moyen, J.F., Janoušek, V., Laurent, O., Bachmann, O., Jacob, F.B., Farina, F., Fiannacca, P., Villaros, A., 2021. Crustal melting vs. fractionation of basaltic magmas: Part 1, granites and paradigms. Lithos 402-403, 106291.

Murphy, J.B., 2020. Appinite suites and their genetic relationship with coeval voluminous granitoid batholiths. International Geology Review 62, 683-713.

Næraa, T., Scherstén, A., Rosing, M.T., Kemp, A.I.S., Hoffmann, J.E., Kokfelt, T.F., Whitehouse, M.J., 2012. Hafnium isotope evidence for a transition in the dynamics of continental growth 3.2 Gyr ago. Nature 485, 627–630.

Najoui, K., Leyreloup, A.F., Monié, P., 2000. Conditions et âges $^{40}Ar/^{39}Ar$ de mise en place des granitoïdes de la zone externe sud du Massif central français: Exemple des granodiorites de St-Guiral et du Liron (Cévennes, France). Bulletin de la Société Géologique de France 171, 495–510.

921 Ni, H., and Keppler, H., 2013. Carbon in silicate melts. In: Hazen, R.M., Jones, A.P., Baross
922 (eds) Carbon in Earth. Reviews in Mineralogy and Geochemistry 75, 251-287.

923 Pearce, J.A., 2008. Geochemical fingerprinting of oceanic basalts with applications to ophiolite
924 classification and the search for Archean oceanic crust. Lithos 100, 14–48.

925 Peccerillo, A., Taylor, S.R., 1976. Geochemistry of Eocene Calc-Alkaline Volcanic Rocks from
926 the Kastamonu Area, Northern Turkey. Contributions to Mineralogy and Petrology 58, 63-81.

927 Pin, C., Duthou, J., 1990. Sources of Hercynian granitoids from the French Massif Central:
928 Inferences from Nd isotopes and consequences for crustal evolution. Chemical Geology 83, 281–
929 296.

930 Pin, C., Paquette, J-L., 1997. A mantle-derived bimodal suite in the Hercynian Belt: Nd isotope
931 and trace element evidence for a subduction-related rift origin of the Late Devonian Brévenne
932 metavolcanics, Massif Central (France). Contributions to Mineralogy and Petrology 129, 222–238.

933 Pin, C., Paquette, J.L., 2002. Sr–Nd isotope and trace element evidence for a Late Devonian
934 active margin in northern Massif-Central (France). Geodinamica Acta 15, 63–77.

935 Plank, T., Langmuir, C.H., 1998. The chemical composition of subducting sediment and its
936 consequences for the crust and mantle. Chemical Geology 145, 325-394.

937 Prelević, D., Akal, C., Foley, S.F., Romer, R.L., Stracke, A., van Den Bogaard, P., 2012.
938 Ultrapotassic mafic rocks as geochemical proxies for post-collisional dynamics of orogenic
939 lithospheric mantle: The case of southwestern Anatolia, Turkey. Journal of Petrology 53, 1019-
940 1055.

941 Rock, N.M.S., 1991. Lamprophyres. Blackie and Son, Glasgow.

942 Sabatier, H., 1991. Vaugnerites: special lamprophyre-derived mafic enclaves in some Hercynian
943 granites from Western and Central Europe. In: Didier, J., Barbarin, B., (eds) Enclaves and
944 Granite Petrology. Elsevier, Amsterdam, pp. 63-81.

945 Sabourdy, G., (1975). Apport de la géochimie à la connaissance de la pétrogenèse des granitoïdes
946 des Cévennes méridionales, Massif central Français. PhD thesis, Université de Clermont-Ferrand.

947 Scaillet, B., Holtz, F., Pichavant, M., 1997. Rheological properties of granitic magmas in their
948 crystallization range. In: Bouchez, J.L., Hutton, D.H.W., Stephens, W.E., (eds) Granite: From
949 Segregation of Melt to Emplacement Fabrics. Petrology and Structural Geology 8, Springer,
950 Dordrecht, pp. 11-29.

951 Scarrow, J.H., Bea, F., Montero, P., Molina, J.F., 2008. Shoshonites, vaugnerites and potassic
952 lamprophyres: Similarities and differences between 'ultra'-high-K rocks. Earth and
953 Environmental Science Transactions of the Royal Society of Edinburgh 99, 159-175.

954 Scholl, D.W., von Huene, R., 2009. Implications of estimated magmatic additions and recycling
955 losses at the subduction zones of accretionary (non-collisional) and collisional (suturing) orogens.
956 In: Cawood, P.A. (ed) Earth Accretionary Systems in Space and Time. Geological Society,
957 London, Special Publications 318, 105-125.

958 Schulmann, K., Lexa, O., Janoušek, V., Lardeaux, J. M., Edel, J. B., 2014. Anatomy of a diffuse
959 cryptic suture zone: an example from the Bohemian Massif, European Variscides. Geology 42,
960 275–278.

961 Solgadi, F., Moyen, J.F., Vanderhaeghe, O., Sawyer, E.W., Reisberg, L., 2007. The relative roles
962 of crustal anatexis and mantle-derived magmas: Generation of synorogenic, Hercynian granites in
963 the Livradois area, French Massif Central. Canadian Mineralogist 45, 581-606.

964 Solomatova, N., Manning, C.E., Lin, J.F., Mao, W.L., 2020. Carbon speciation and solubility in
965 silicate melts. In: Manning, C.E., Lin, J.F., Mao, W.L. (eds) Carbon in Earth's Interior.
966 Geophysical Monograph Series 249, 179–194. https://doi.org/10.1002/9781119508229.ch16

967 Spencer, C.J., Cawood, P.A., Hawkesworth, C.J., Prave, A.R., Roberts, N.M.W., Horstwood,
968 M.S.A., Whitehouse, M.J., EIMF., 2015. Generation and preservation of continental crust in the
969 Grenville Orogeny. Geoscience Frontiers 6, 357-372.

970 Spencer, C.J., Cavosie, A.J., Raub, T.D., Rollinson, H., Jeon, H., Searle, M.P., Miller, J.A.,
971 McDonald, B.J., Evans, N.J., 2017. Evidence for melting mud in Earth's mantle from extreme
972 oxygen isotope signatures in zircon. Geology 45, 975–978.

973 Stampfli, G.M., Hochard, C., Vérard, C., Wilhem, C., von Raumer, J. 2013. The formation of
974 Pangea. Tectonophysics 593, 1–19.

975 Soder, C.G., Romer, R.L., 2018. Post-collisional potassic–ultrapotassic magmatism of the
976 Variscan Orogen: implications for mantle metasomatism during continental subduction. Journal
977 of Petrology 59, 1007-1034.

978 Storck, J.C., Laurent, O., Karakas, O., Wotzlaw, J.F., Galli, A., Sinigoi, S., Bachmann, O.,
979 Chelle-Michou, C., 2021. Mantle versus crustal contributions in crustal-scale magmatic systems
980 (Sesia Magmatic System, northern Italy) from coupling Hf isotopes and numerical modelling.
981 Contributions to Mineralogy and Petrology 176, 95.

Stracke, A., 2012. Earth's heterogeneous mantle: A product of convection-driven interaction between crust and mantle. Chemical Geology 330-331, 274-299.

Su, H.M., Jiang, S.Y., Zhang, D.Y., Wu, X.K., 2017. Partial melting of subducted sediments produced Early Mesozoic calc-alkaline lamprophyres from Northern Guangxi Province, South China. Scientific Reports 7, 4864, https://doi.org/10.1038/s41598-017-05228-w.

Sun, S.S., McDonough, W.F., 1989. Chemical and Isotopic Systematics of Oceanic Basalts: Implications for Mantle Composition and Processes. In: Saunders, A.D., Norry, M.J., (eds.), Magmatism in the Ocean Basins, Geological Society of London, Special Publications 42, 313-345.

Sun, J-F., Yang, J-H., Wu, F-Y., Li, X-H., Yang, Y-H., Xie, L-W., Wilde, S.A., 2010. Magma mixing controlling the origin of the Early Cretaceous Fangshan granitic pluton, North China Craton: *In situ* U–Pb age and Sr-, Nd-, Hf- and O-isotope evidence. Lithos 120, 421-438.

Tabaud, A. S., Janousek, V., Skrzypek, E., Schulmann, K., Rossi, P., Whitechurch, H., Guerrot, C. & Paquette, J. L. 2015. Chronology, petrogenesis and heat sources for successive Carboniferous magmatic events in the Southern-Central Variscan Vosges Mts (NE France). Journal of the Geological Society, 172, 87-102.

Talbot, J.Y., Chen, Y., Faure, M., 2005. A magnetic fabric study of the Aigoual–Saint Guiral–Liron granite pluton (French Massif Central) and relationships with its associated dikes. Journal of Geophysical Research 110, B121106.

1001 Tang, M., Wang, X.L., Shu, X.J., Wang, D., Yang, T., Gopon, P., 2014. Hafnium isotopic
1002 heterogeneity in zircons from granitic rocks: Geochemical evaluation and modeling of "zircon
1003 effect" in crustal anatexis. Earth and Planetary Science Letters 389, 188-199.

1004 Tappe, S., Smart, K., Torsvik, T., Massuyeau, M., Wit, M., 2018. Geodynamics of kimberlites on
1005 a cooling Earth: Clues to plate tectonic evolution and deep volatile cycles. Earth and Planetary
1006 Science Letters 484, 1-14.

1007 Taylor, H.P., Sheppard, S.M.F., 1986. Igneous rocks: I. Processes of isotopic fractionation and
1008 isotope systematics, In: Valley, J.W., Taylor, H.P., O'Neil, J.R. (eds) Stable Isotopes in High
1009 Temperature Geological Processes, , Mineralagical Society of America, Washington. 227-271

1010 Thibault, Y., Edgar, A.D., Lloyd, F.E., 1992. Experimental investigation of melts from a
1011 carbonated phlogopite lherzolite: Implications for metasomatism in the continental lithospheric
1012 mantle. American. Mineralogist.77, 784–794.

1013 Turpin, L., Velde, D., Pinte, G., 1988. Geochemical comparison between minettes and kersantites
1014 from the Western European Hercynian Orogen: trace element and Pb-Sr-Nd isotope constraints
1015 on their origin. Earth and Planetary Science Letters 87, 73–86.

1016 Vanderhaeghe, O., Laurent, O., Gardien, V., Moyen, J.F., Gébelin, A., Chelle-Michou, C.,
1017 Couzinié, S., Villaros, A., Bellanger, M., 2020. Flow of partially molten crust controlling
1018 construction, growth and collapse of the Variscan orogenic belt: The geologic record of the
1019 French Massif Central. BSGF Earth Sciences Bulletin 191, 25.

1020 Villaros, A., Buick, I.S., Stevens, G., 2012. Isotopic variations in S-type granites: an inheritance
1021 from a heterogeneous source? Contributions to Mineralogy and Petrology 163, 243-257.

1022 Villaros, A., Laurent, O., Couzinié, S., Moyen, J.F., Mintrone, M., 2018. Plutons and domes: The
1023 consequences of anatectic magma extraction – example from the south-eastern French Massif
1024 Central. Internationa Journal of Earth Science 107, 2819–2842.von Raumer, J.F., Finger, F.,
1025 Veselá, P., Stampfli, G.M., 2014. Durbachites–Vaugnerites – a geodynamic marker in the central
1026 European Variscan orogen. Terra Nova 26, 85-95.

1027 Wang, D., Guo, J., Romer, R.L., Liu, F., Ouyang, D., 2021. Coeval shoshonitic and calc-alkaline
1028 mantle-derived magmatism in an ancient continental arc root. Contributions to Mineralogy and
1029 Petrology 176, 57, https://doi.org/10.1007/s00410-021-01812-6.

1030 Warr, L.N., 2021. IMA–CNMNC approved mineral symbols. Mineralogical Magazine 85, 291-
1031 320.

1032 Williamson, B.J., Downes, H., Thirlwall, M.F., 1992. The relationship between crustal magmatic
1033 underplating and granite genesis – an example from the Velay Granite. Transactions of the Royal
1034 Society of Edinburgh-Earth Sciences 83, 235-245.

1035 Workman, R.K., Hart, S.R., 2005. Major and trace element composition of the depleted MORB
1036 mantle (DMM). Earth and Planetary Science Letters 231, 53– 72.

1037 Yamasaki, T. 2022. Magma hybridization and crystallization in coexisting gabbroic and granitic
1038 bodies in the mid-crust, Akechi district, central Japan. Mineralogy and Petrology 116, 189-228.

1039 Yang, J-H., Wu, F-Y., A. Wilde, S.A., Xie, L-W., Yang, Y-H., Liu, X-M., 2007. Tracing magma
1040 mixing in granite genesis: in situ U–Pb dating and Hf-isotope analysis of zircons. Contributions to
1041 Mineralogy and Petrology 153, 177–190.

1042

1043 **Figure Captions**

1044 Figure 1. (a) General location of Variscan belt in Western–Central Europe. (b) Geological map of
1045 the eastern French Massif Central modified from Moyen et al. (2017). Post-collisional mafic
1046 magmatic rocks (vaugnerites) occurrences from Couzinié et al. (2016). (c) Geological map of
1047 Aigoual granite and composite dykes modified from Talbot et al. (2005). At the scale illustrated,
1048 it is not possible to differentiate the different lamprophyric components of the dykes from the
1049 granites.

1050

1051 Figure 2. Selected field photos illustrating key field relations (a) A section of aomposite dyke
1052 with the field of view orientated perpendicular to the strike of the dyke. A typical gradational
1053 contact from lamprophyre (left) to granite (right) is illustrated, also showing the increasing
1054 proportion and size of phenocrysts of K-feldspars; (b) Field relationships between lamprophyre
1055 and granite showing that two different generations of lamprophyre dykes intrude a granite dyke.
1056 The contacts in this case are sharp with no evidence of mingling; (c) Aigoual granite with a

1057 typical rounded enclave of lamprophyre cut by a later thin aplitic dyke. The larger pale coloured
1058 inclusions in the enclave represent partially resorbed K-feldspar phenocrysts.
1059
1060 Figure 3. Photomicrographs and BSE images of lamprophyres and granites from composite
1061 dykes. (a–b) Euhedral–subhedral biotite in lamprophyre; (c) Interstitial dolomite in lamprophyre
1062 associated with euhedral quartz, plagioclase and biotite; (d) Calcite associated with biotite in
1063 granite; (e) Ocellar carbonate and microcrysts of K-feldspar in lamprophyre; (f) Plagioclase and
1064 biotite phenocryst in lamprophyre; (g–h) BSE images with compositional variation in
1065 biotite/phlogopite from lamprophyre; (i) Fine-grained granite from composite dykes; (j–l)
1066 Textural variation in granite from composite dykes with phenocrysts of zoned plagioclase, K-
1067 feldspar (j), quartz (k) and corroded megacryst of K-feldspar (l). Mineral abbreviations from
1068 Warr (2021).
1069
1070 Figure 4. (a) Al – Mg – Fe^{2+} ternary diagram showing compositional variations of biotite to
1071 phlogopite. Minettes and lamproites fields after Rock (1991). (b) Al_2O_3 vs. FeO^T and (c) Al_2O_3
1072 vs. TiO_2 discrimination diagram for micas after Mitchell and Bergman (1991). Abbreviations: Es
1073 = Eastonite, Ph = Phlogopite, Sd = Siderophyllite, and An = Annite.
1074
1075 Figure 5. Zircon U–Pb Tera–Wasserburg concordia diagrams for composite dykes and Aigoual
1076 granite. Data-point error ellipses are 2σ.
1077
1078 Figure 6. Diagram of $^{206}Pb/^{238}U$ ages (Ma) versus $\varepsilon^{Hf}_{(t)}$ from zircons of composite dykes and
1079 Aigoual granite. $\varepsilon^{Hf}_{(t)}$ lower and upper limit for Depleted Mantle (DM) are from Næraa et al.

(2012) and Griffin et al. (2004). The KDE curve (light pink) portrays the $^{206}Pb/^{238}U$ age distribution used to calculate the Concordia ages.

Figure 7. (a) SiO_2 vs. K_2O classification diagram of Peccerillo and Taylor (1976); (b) A/CNK vs. A/NK diagram.

Figure 8. Whole-rock major- and trace-element compositions of lamprophyre and granite from composite dykes and Aigoual granite.

Figure 9. (a) Primitive mantle-normalized rare earth element (REE) patterns from Sun and McDonough (1989); (b) Multi-element normalized to Primitive mantle from Sun and McDonough (1989). GLOSS composition from Plank and Langmuir (1998); PCMM – post-collisional mafic magmatism from FMC of Couzinié et al. (2016); CAL – China – Calc-alkaline lamprophyre derived by partial melting of subducted sediments from Su et al. (2017).

Figure 10. (a) SiO_2 versus $\delta^{18}O$ quartz; (b) log(Ni + Cr) versus $\delta^{18}O$ quartz; (c) $\delta^{18}O$ quartz versus $\delta^{18}O$ feldspar. Quartz–feldspar isotherms for 550 ºC and 950 ºC calculated using the calibrations of Chiba et al. (1989).

Figure 11. (a) Nb/Yb vs. Th/Yb diagram after Pearce (2008) suggesting the involvement of continental crust in the formation of the magmas that produced the composite dykes. (b) Ba/Rb vs. Rb/Sr diagram (after Furman and Graham, 1999) suggesting the presence of phlogopite in the mantle source region as a consequence of the metasomatism by a crustal component; (c) La/Yb

vs. Nb/La diagram (Abdel and Nassar, 2004). Granites are also plotted (in pale colors), as they are comagmatic and may be derived from similar source rocks. Primitive mantle (PM) values from Hofmann (1988).

Figure 12. Histogram of $\delta^{18}O$ quartz analyses from this study. Mantle whole-rock O isotopic value (~5.7‰) from Eiler (2001); I- and S-type granites from Harris et al. (1997) and peraluminous granite from Oman-United Arab Emirates (UAE) ophiolite from Spencer et al. (2017).

Figure 13. (a) Results of mixing models between mantle ($\delta^{18}O$ = 5.7‰ and $^{87}Sr/^{86}Sr_{initial}$ = 0.703) and three different contaminants all characterised by $^{87}Sr/^{86}Sr_{initial}$ = 0.715 (GLOSS, Plank and Langmuir 1998) but having different $\delta^{18}O$ values: carbonate-bearing sediments (28‰), pelagic clays (20‰) and average continental crust (15‰) (Eiler, 2001).

Figure 14. (a) $\varepsilon^{Nd}_{initial}$ vs. $^{87}Sr/^{86}Sr_{initial}$ plot for composite dykes and Aigoual granite. Initial ratios calculated at 311 Ma. Lithospheric mantle melting field from Davis and Blanckenburg (1995); Vaugnerites French Massif Central (FMC) from Moyen et al. (2017); Variscan lamprophyres from Soder and Romer (2018). The mixing calculations used the Variscan mantle composition from Pin and Paquette (1997), GLOSS from Plank and Langmuir (1998) and FMC paragneiss compositions from Moyen et al. (2017); (b) $\varepsilon^{Hf}_{initial}$ vs. $\varepsilon^{Nd}_{initial}$ plot for composite dykes and Aigoual granite. Data from MORB and OIB are taken from Stracke (2012) and mantle array regression line from Chauvel et al. (2008). Global kimberlites field from Tappe et al. (2018). DM = depleted mantle; OIB = ocean island basalt.

Figure 15. (a) La/Yb vs. Yb plot with batch melting modelsfor phlogopite-bearing spinel and garnet peridotite. The calculated sources correspond to Depleted Mantle (Workam and Hart 2005) mixed with 20% to 30% GLOSS (Plank and Langmuir 1998). Modal proportions in the residue are recalculated from Condamine and Médard (2014) for spinel peridotite (olivine 0.69, orthopyroxene 0.15, clinopyroxene 0.08, phlogopite 0.07, spinel 0.01) and Thibault et al. (1992) for garnet peridotite (olivine 0.25, orthopyroxene 0.50, clinopyroxene 0.15, phlogopite 0.03, garnet 0.07). Partition coefficients for mafic and intermediate rocks from Laurent (2012). (b) Multielement patterns of lamprophyres and granites and calculated compositions generated by 5, 10 and 20% of partial melting of a phlogopite-bearing spinel peridotite source. Black and gray continuous lines represent partial melting of a calculated source with DM + 20% GLOSS and blue dashed lines of DM + 35% GLOSS. Partition coefficients from mafic and intermediate rocks from Laurent (2012). The melt composition from calculated source replicates the multi-element patterns exhibited by lamprophyres and granites well, except for the LREE.

Supplementary Material

Supplementary Figure 1. BSE images and X-ray maps of three different magmatic textures of carbonate.

Supplementary Figure 2. (a) Ternary diagram of classification of feldspars; (b) Ternary diagram of classification of clinopyroxene; (c) (d) Amphibole classification.

Supplementary Figure 3. Selected CL images of zircon from composite dykes and Aigoual granite with U–Pb age and ε^{Hf} values.

Supplementary Data 1. Analytical methods.

Supplementary Data 2. Coordinates and lithologies of the samples taken from composite dykes in the Aigoual granite.

Supplementary Data 3

Supplementary Data 3 Table S1. Whole-rock major- (wt.%) and trace-element (ppm) compositions of composite dykes from Aigoual granite, French Massif Central.

Supplementary Data 3 Table S2. Whole-rock Sr, Nd, Hf isotopes.

Supplementary Data 3 Table S3. $\delta^{18}O$ values from quartz and feldspar from lamprophyre and granite of composite dykes and Aigoual granite (AG14A).

Supplementary Data 4

Supplementary Data 4 Table S1. Zircon LA-SF-ICP-MS U–Pb geochronology data.

Supplementary Data 4 Table S2. Analytical results for zircon Lu–Hf isotopes determinations.

Supplementary Data 5

Supplementary Data 5 Table S1. Mineral chemistry of biotite/phlogopite

Supplementary Data 5 Table S2. Mineral chemistry of feldspars

Supplementary Data 5 Table S3. Mineral chemistry of clinopyroxene

Supplementary Data 5 Table S4. Mineral chemistry of amphibole

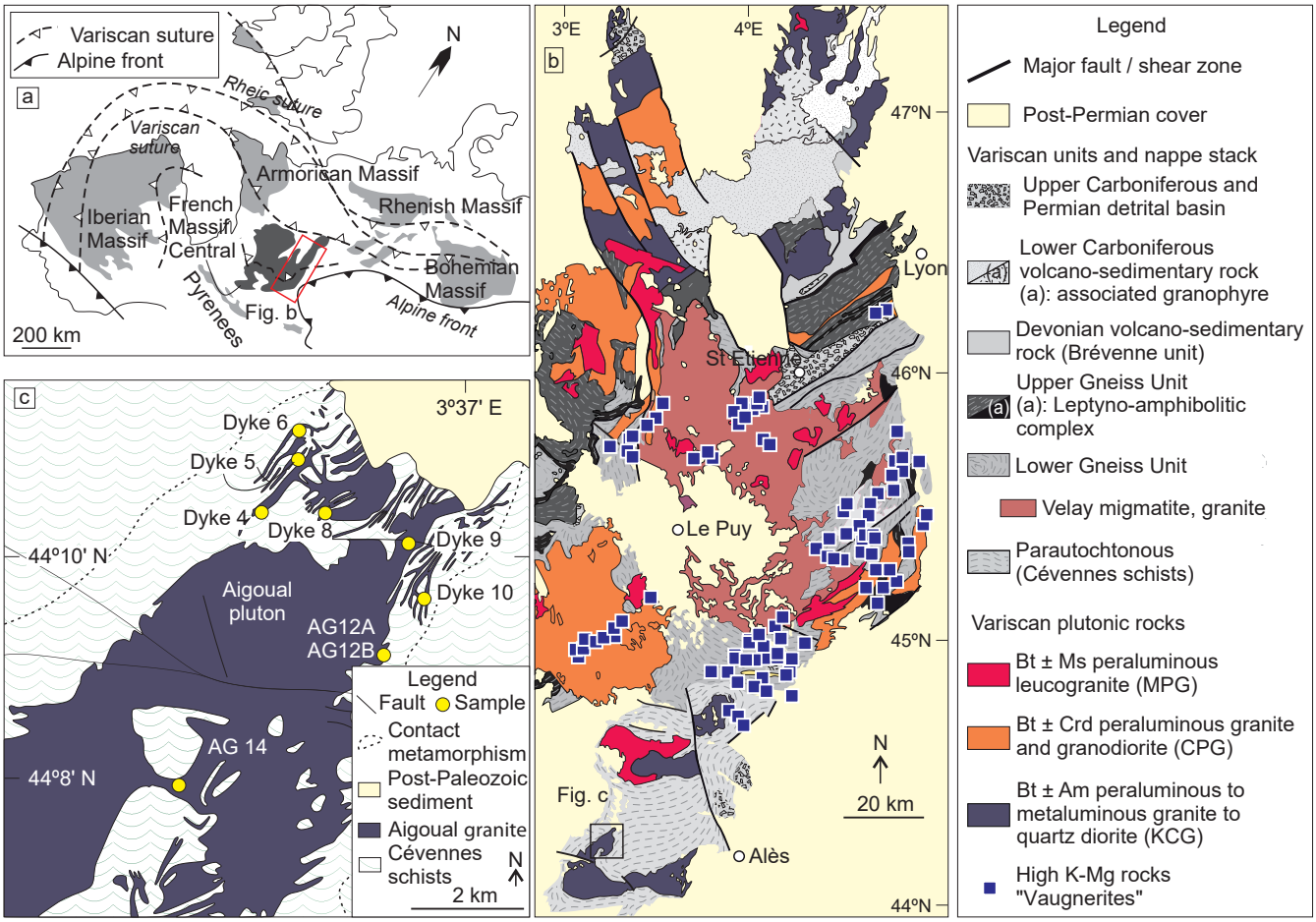

Figure

Click here to access/download;Figure;0 Figure 3.pdf

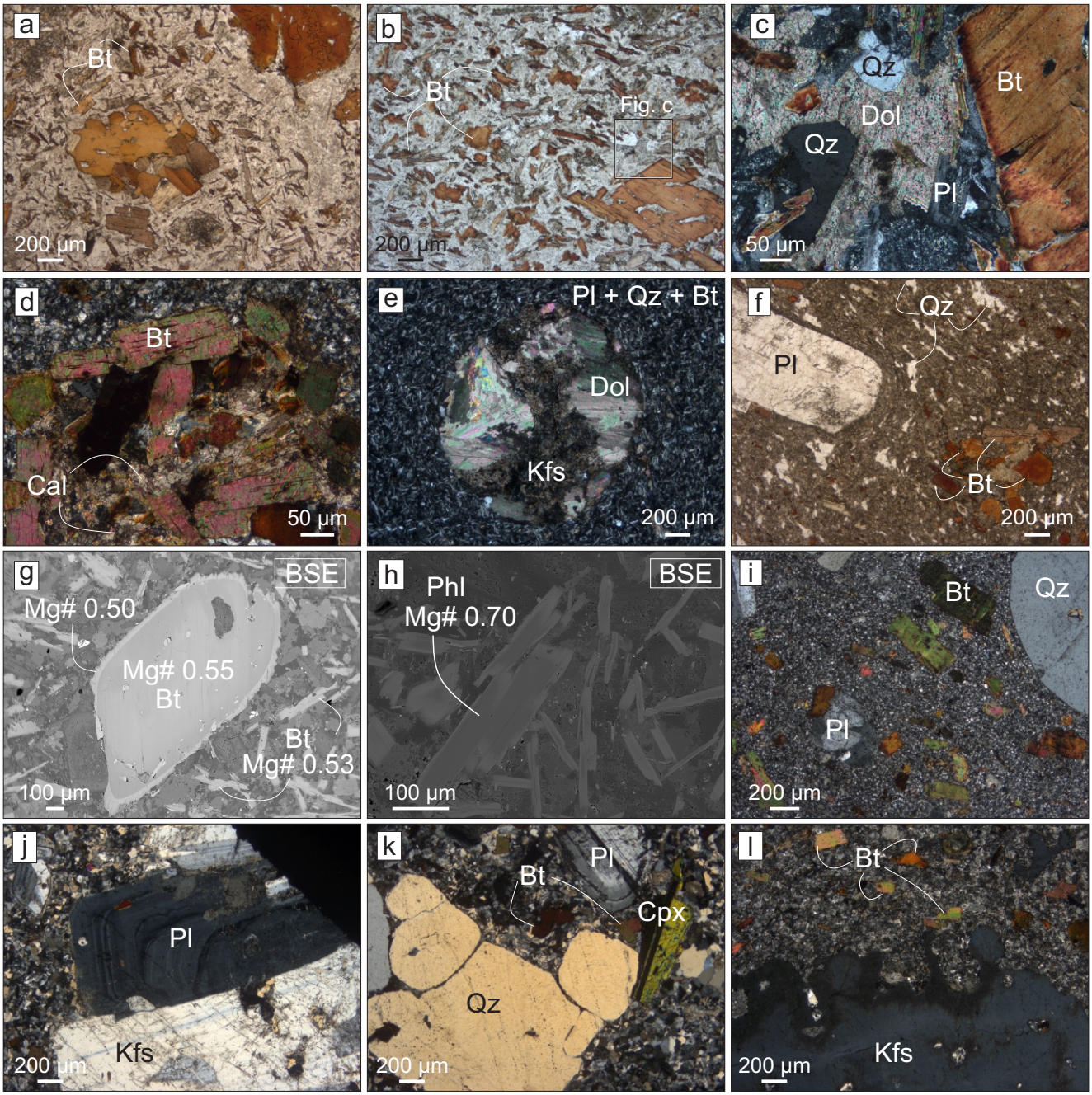

Figure

Click here to access/download;Figure;0 Figure 4.pdf

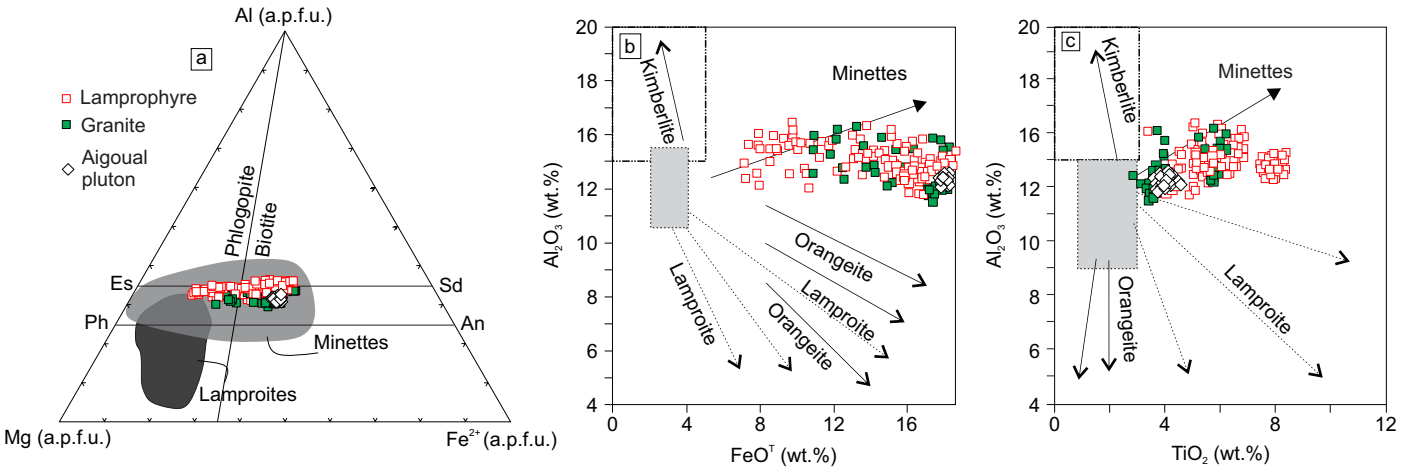

Figure

Click here to access/download;Figure;0 Figure 5.pdf

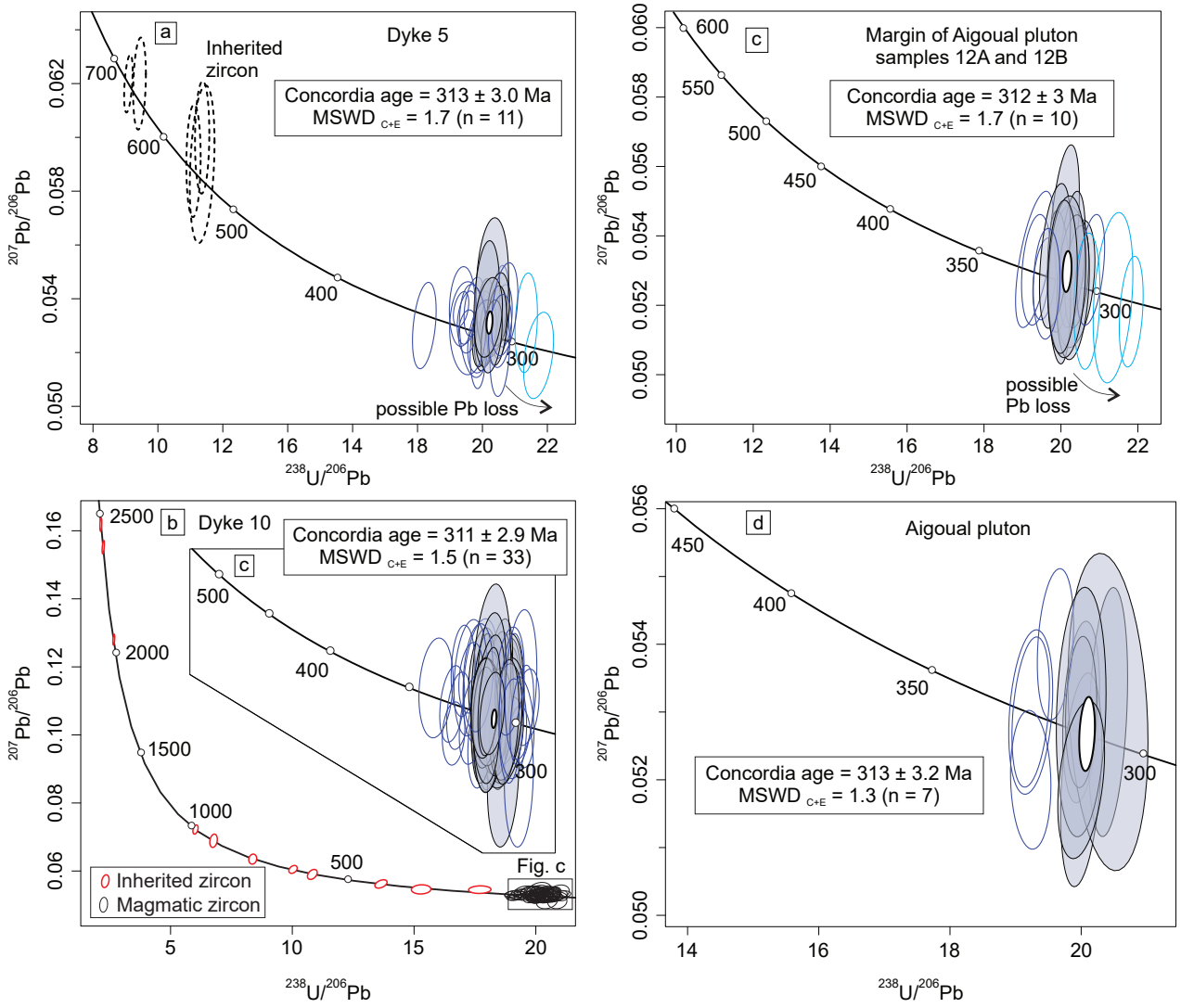

Figure

Click here to access/download;Figure;0 Figure 6.pdf

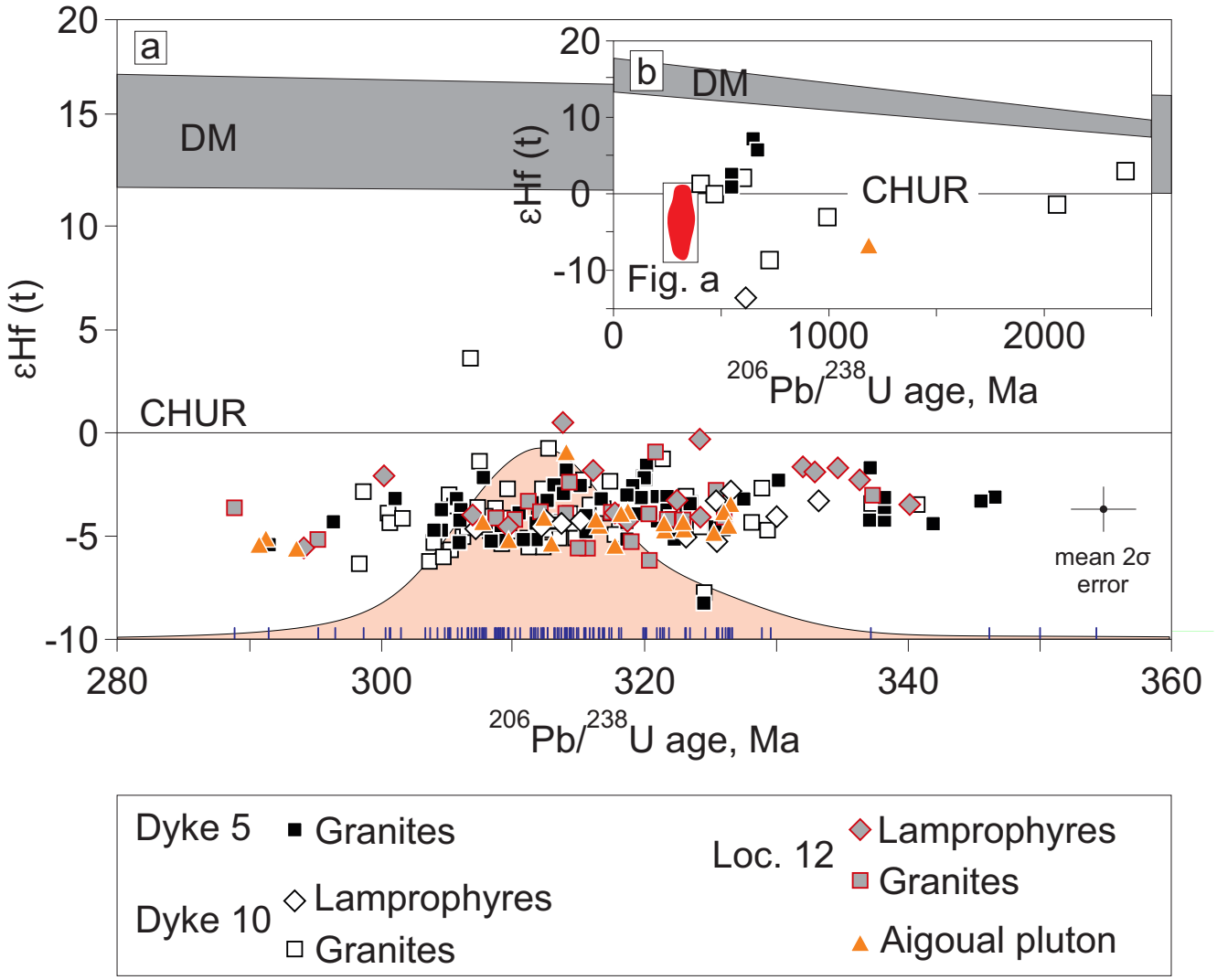

Figure

Click here to access/download;Figure;0 Figure 7.pdf

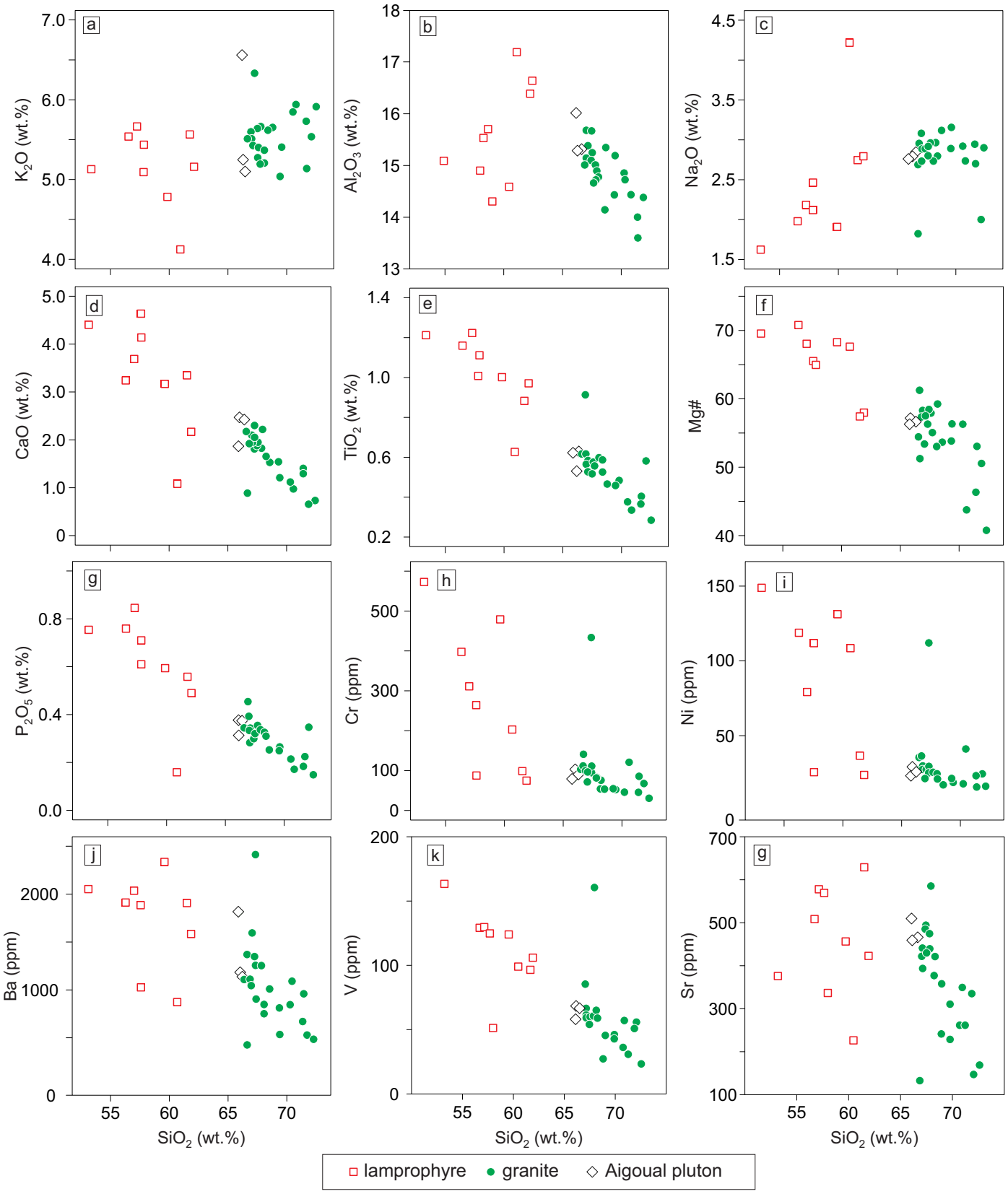

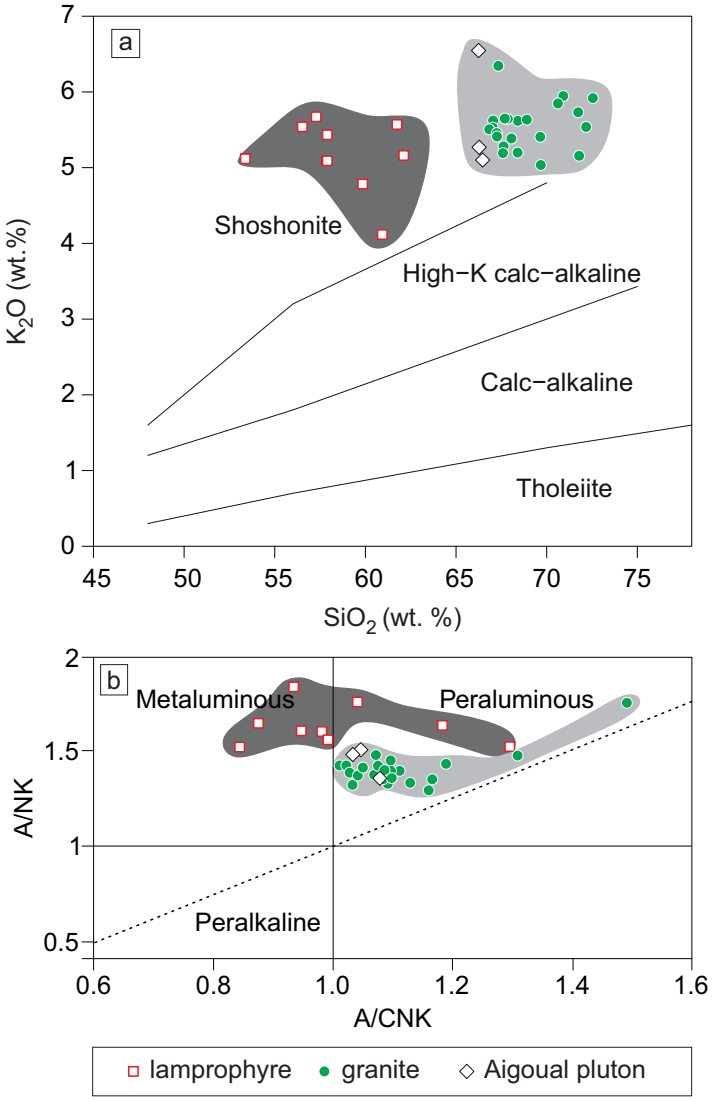

Figure

Click here to access/download;Figure;0 Figure 9.pdf

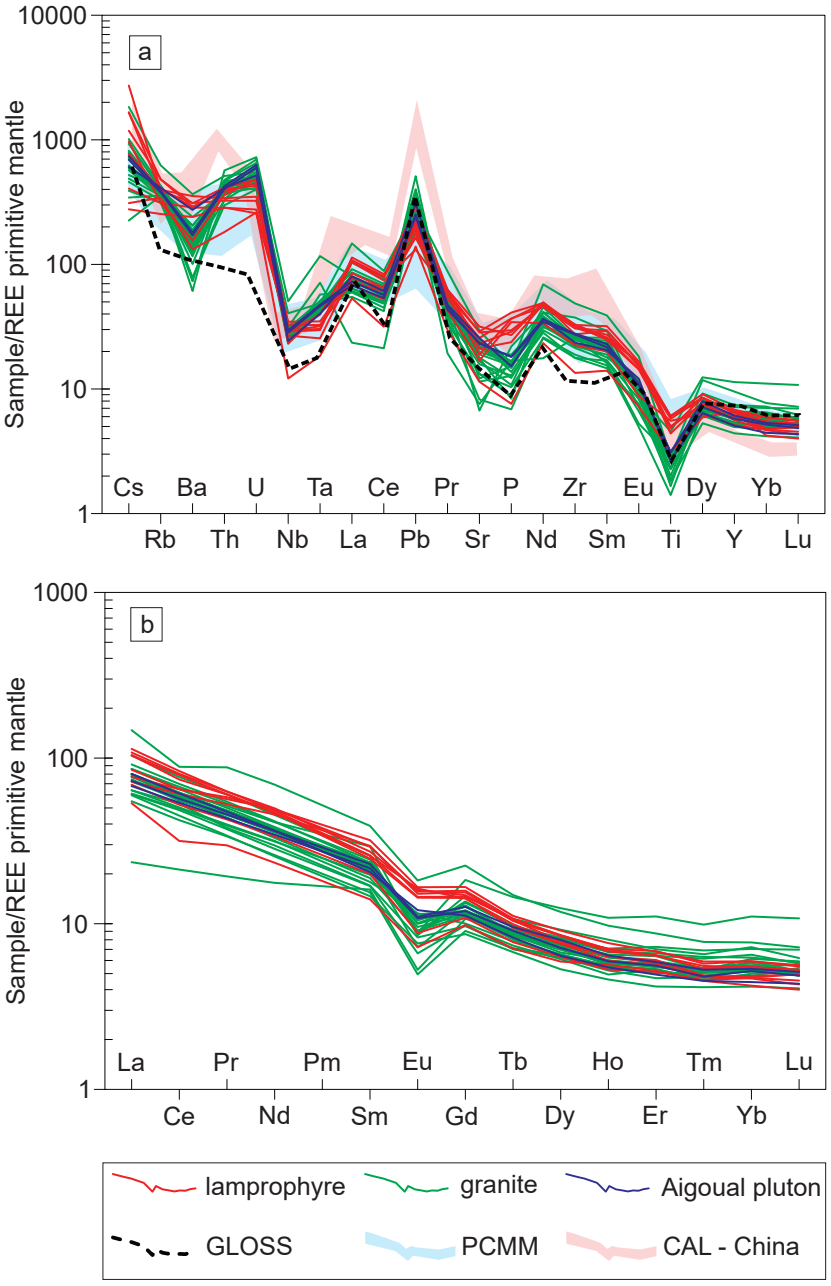

Figure

Click here to access/download;Figure;0 Figure 10.pdf

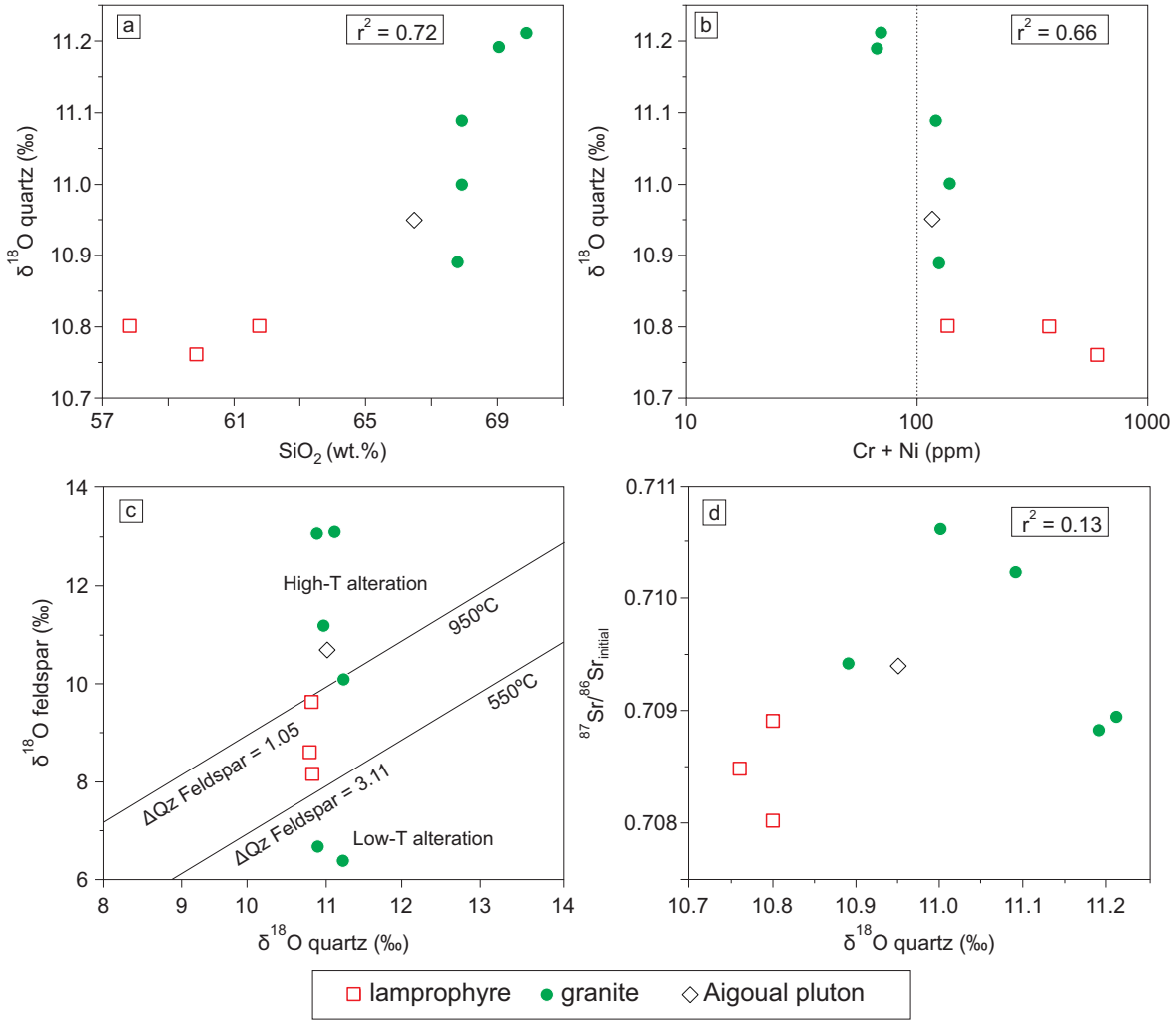

Figure

Click here to access/download;Figure;0 Figure 11.pdf

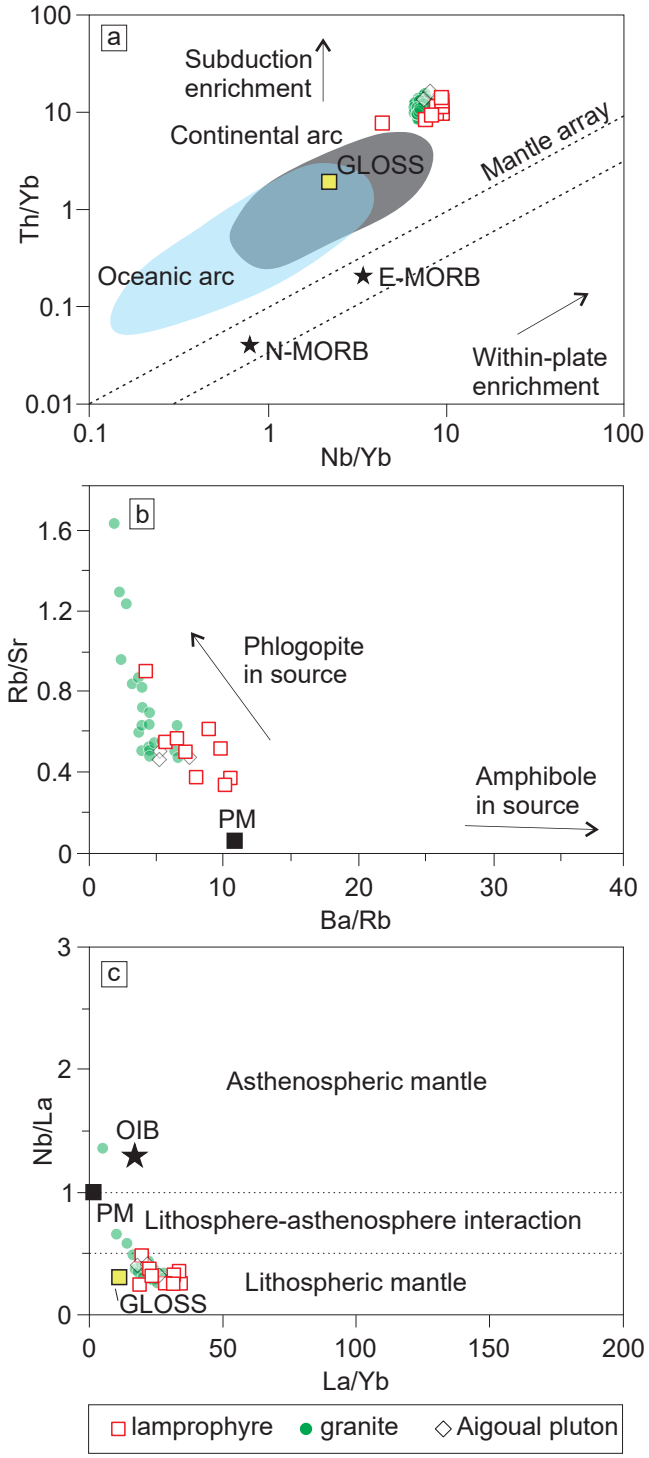

Figure

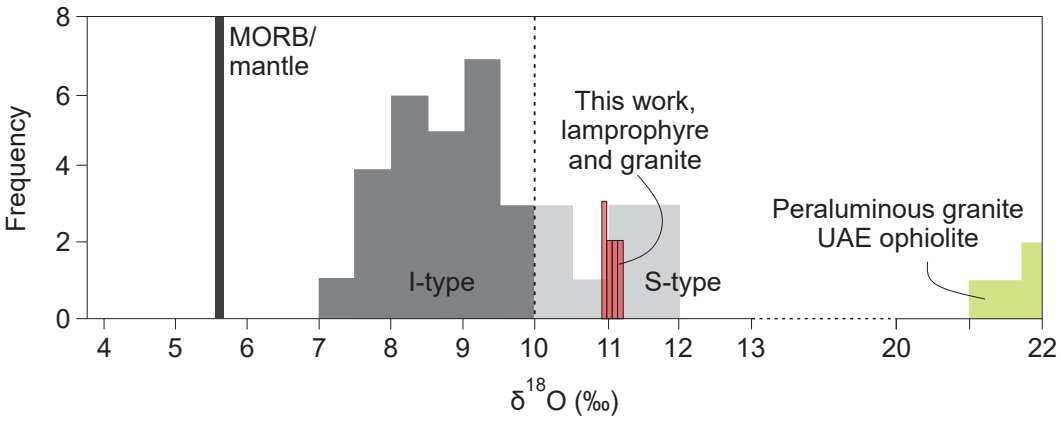

Figure

Click here to access/download;Figure;0 Figure 13.pdf

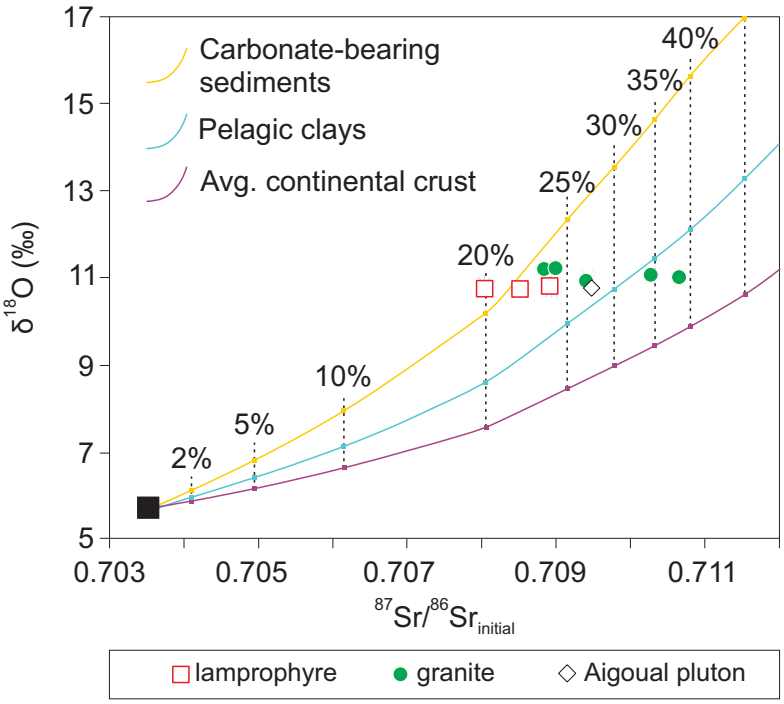

Figure

Click here to access/download;Figure;0 Figure 14.pdf

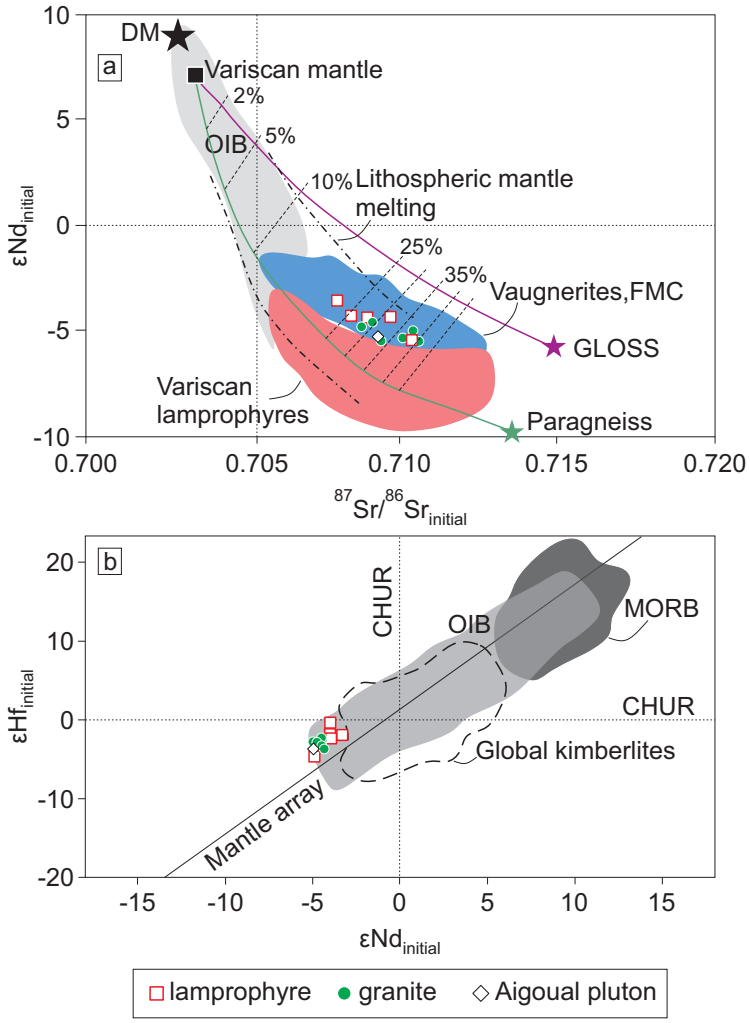

Figure

Click here to access/download;Figure;0 Figure 15.pdf

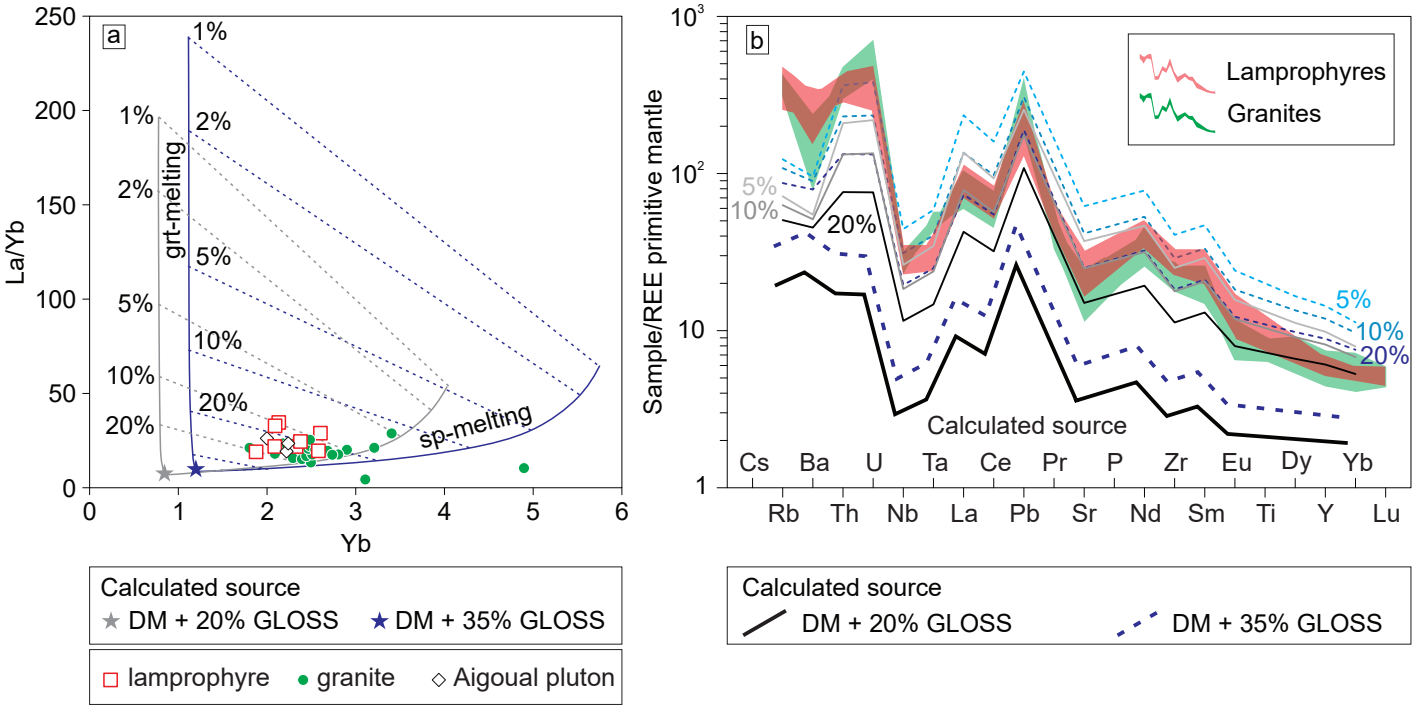

Calculated source
★ DM + 20% GLOSS ★ DM + 35% GLOSS

□ lamprophyre ● granite ◇ Aigoual pluton

Calculated source
DM + 20% GLOSS DM + 35% GLOSS

Declaration of interests

☒ The authors declare that they have no known competing financial interests or personal relationships that could have appeared to influence the work reported in this paper.

☐The authors declare the following financial interests/personal relationships which may be considered as potential competing interests:
